Research Article

Adakite genesis and plate convergent process: Constraints from whole rock and mineral chemistry, Sr, Nd, Pb isotopic compositions and U-Pb ages of the Lakhshak magmatic suite, East Iran

Mehdi Rezaei-Kahkhaei [a], Fernando Corfu [b,*], Carmen Galindo [c,1], Reza Rahbar [a], Habibollah Ghasemi [a]

[a] Department of Petrology and Economic Geology, Faculty of Earth Sciences, Shahrood University of Technology, Shahrood, Iran
[b] Department of Geosciences and CEED, University of Oslo, PB1047 Blindern, N-0316 Oslo, Norway
[c] Departmento de Petrología y Geoquímica, Universidad Complutense–IGEO (UCM-CSIC), C/ José Antonio Novais n° 2, 28040 Madrid, Spain

ARTICLE INFO

ABSTRACT

The genesis of Eocene to Early Oligocene plutons and dykes emplaced in the suture zone between two colliding continental blocks in southeastern Iran has been the subject of debate concerning the processes that formed magmas and influenced their intrusive history. We report geological, geochemical, mineralogical and isotope evidence that constrains the origin of the Lakhshak plutonic complex. SiO_2 contents in the granodioritic pluton and dacite dykes average 67 wt%, and in the monzodiorite dykes 53 wt%. Based on $(La/Yb)_N$ vs. Yb_N the rocks correspond to adakites, originating from 10 to 25% melting of garnet amphibolite. The high Al_2O_3 (14.95–17.15 wt%), Sr (442–1385 ppm) and Ba (601–1935 ppm) contents and relatively high La/Yb (25–45) and Sr/Y (35–57), but low Yb (mostly <1.6 ppm) and Y (mostly <18.2 ppm) are also features typical of adakitic rocks. Zircon and titanite from two samples of the pluton yield U-Pb ages of 29.98 ± 0.08 and 29.90 ± 0.05 Ma, a monzodiorite dyke yields 29.02 ± 0.10 Ma, and a dacite dyke 29.39 to 27.96 Ma. These ages confirm that the magmatism was post-collisional. The monzodiorite and dacite dykes have $(^{87}Sr/^{86}Sr)_i = 0.7053$–0.7056 and $\varepsilon Nd_i = -1.1$ to 2.2 (except one sample with $\varepsilon Nd_i = -8.6$), which limit the extent of crustal assimilation and plot along a mixing array between Sistan ophiolites and the country rocks of the pluton. This is consistent with an origin from oceanic slab melts variously mixed with melts from flysch sediments. Isotope compositions of Sr, Nd and Pb, xenocrystic zircons, and magma mixing and mingling textures support such a process. Thermobarometry on various minerals indicates a continuum of crystallization stages during magma ascent, with pyroxene formed at 8 kbar, followed by amphiboles, which record conditions decreasing from 1166 °C / 7.8 kbar to 933 °C / 4.0 kbar. Tectonically, the Lakhshak adakites were most likely the consequence of post-collisional delamination that led to melting of Sistan oceanic lithosphere and its interaction with melts from pelagic sediments.

1. Introduction

Adakites are mostly silicic rocks ($SiO_2 > 56\%$) with >3.5% Na_2O, $K_2O/Na_2O \sim 0.4$, >15% Al_2O_3, Sr/Y > 40 and La/Yb >20, <18 ppm Y, <1.8 ppm Yb, and low amounts of high field strength elements (HFSE, including Ti, Nb, Ta) (Defant and Drummond, 1990). They are inferred to originate through partial melting of subducted metabasaltic crust. The characteristically high Sr/Y (and La/Yb) of adakites is attributed to the presence of garnet in the residues (eclogite or garnet amphibolite;

Martin et al., 2005; Moyen, 2009). Proposed sources and settings include very young and warm oceanic lithosphere (<25 Ma; Defant and Drummond, 1990; Sajona et al., 1996; Martin, 1999), oceanic ridges (e.g., Aguillón-Robles et al., 2001), fast subduction (e.g., Molnar and England, 1990), flat subduction due to anomalous heating of the leading edge of the slab (e.g., Bourdon et al., 2002), termination of subduction (Sajona et al., 1996) or slab windows with hot asthenosphere in direct contact with the plate edge (e.g., Yogodzinski et al., 1995).

Many adakites have higher Ni and Cr contents than expected for
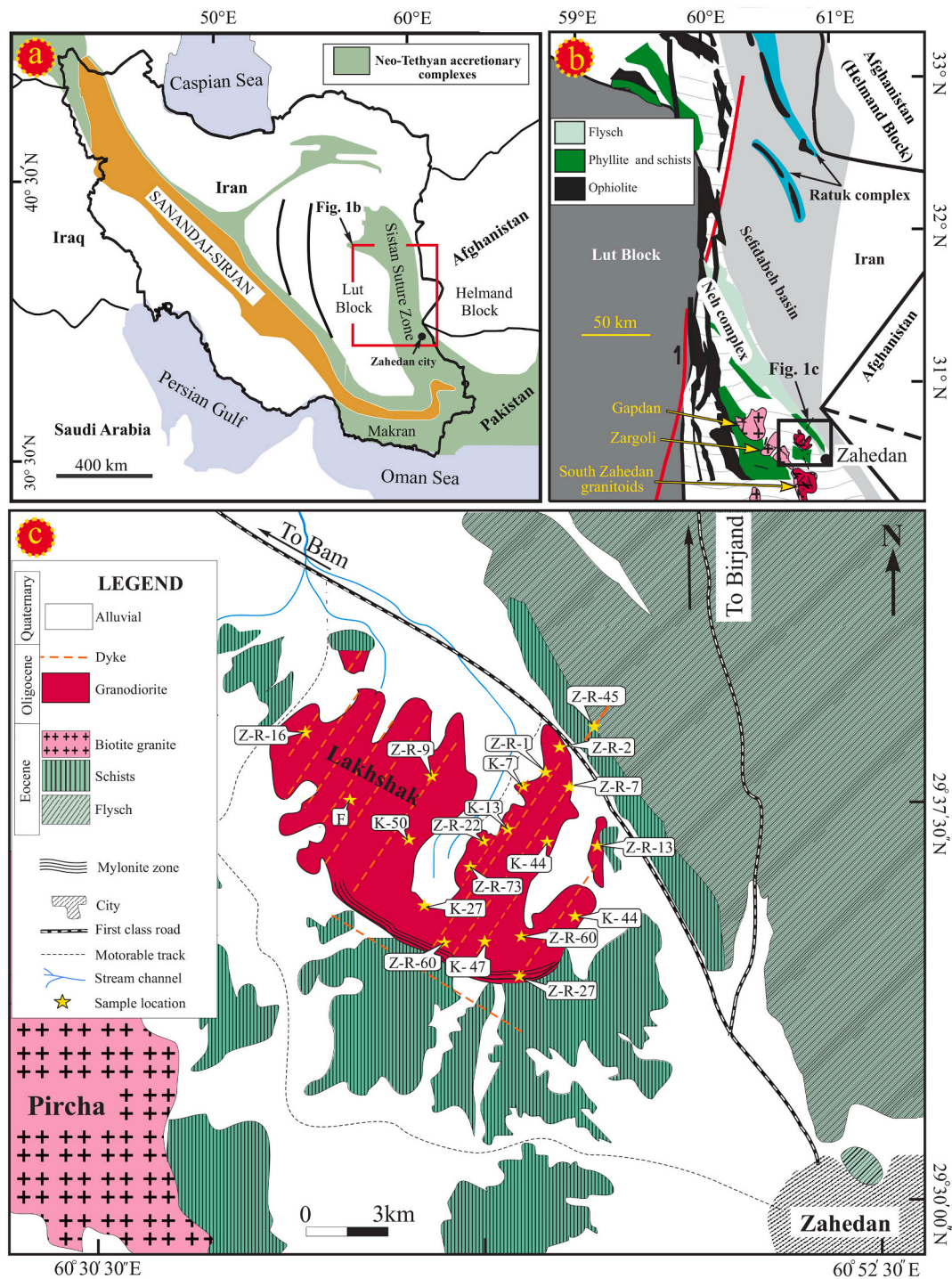
Fig. 1. (a) Tectonic overview of Iran (modified after Bröcker et al., 2013). (b) Major geological subdivisions of the Sistan Suture Zone and the location of Zahedan-Saravan granitoids (modified after Tirrul et al., 1983). (c) Geological map of the Lakhshak pluton showing the location of the samples used for whole rock major, trace elements and isotopic analyses, mineral chemistry and U-Pb dating (Tables 1–7).

pristine slab melts, indicating interaction of the magma with mantle wedge peridotite on their way toward the surface (e.g., Martin et al., 2005; Moyen, 2009). The adakitic signatures could also be generated by fractionation of mafic minerals from non-adakitic melts (e.g., Kolb et al., 2013), fractionation of amphibole during the differentiation of a basaltic arc magma formed in a mantle wedge previously metasomatized by slab fluids, or basaltic arc magma that assimilated crustal materials (Richards and Kerrich, 2007); melting of thickened mafic arc-crust (e.g., Wang et al., 2005) or delaminated basaltic lower continental crust (Gao et al.,

2004), and mixing between crust-derived felsic melt and mantle-derived mafic melt (e.g., Wang et al., 2019).

The Lakhshak pluton and related dykes in the Neh Complex in southeastern Iran have adakitic characteristics. In this paper we use structural relationships, geochemistry, mineral chemistry and geochronology to document the petrogenesis of this adakitic suite, which was associated with subduction of the Sistan Ocean, a branch of Neo-Tethys, and its Cenozoic closure. The U-Pb ages reported below show that the parent magma of the Lakhshak pluton was emplaced in the suture after
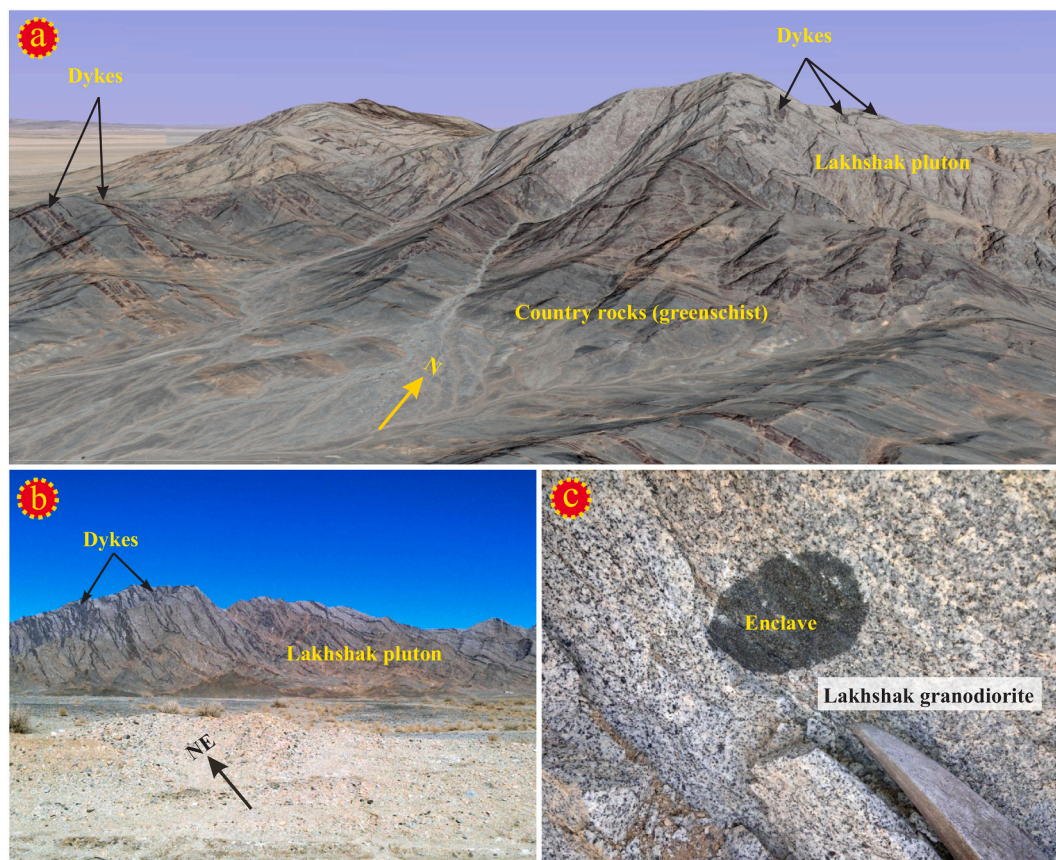
Fig. 2. Photographs of the Lakhshak pluton, its country rocks and the related dykes. (b) Numerous NE-striking dykes occupy 20 to 30% of the pluton volume. (c) Mafic microgranular enclaves in Lakhshak granodiorite.

collision of the Lut and Helmand continental blocks. The geochemical and isotope data show that the Sistan oceanic slab and low-grade flysch-type metasedimentary assemblage played the main role as source materials for the genesis the pluton.

2. Geological setting

2.1. The Sistan suture zone

The Lut and Helmand continental blocks consist of Neoproterozoic to Paleozoic basement and granulite facies metamorphic rocks (Bagheri and Stampfli, 2008). Rifting between these blocks formed a small branch of the Neo-Tethys Ocean, the Sistan Ocean, oriented N-S for >700 km (Fig. 1). Rifting may have started during the Early (to Middle) Cretaceous, inferred from Orbitolina limestone (Barremian to Aptian) and zircon U-Pb ages of 113 ± 1 and 107 ± 1 Ma for the ophiolite (Babazadeh and De Wever, 2004; Zarrinkoub et al., 2012). Formation of the ophiolites and ophiolitic melanges was followed by deposition of Late Cretaceous-Eocene flysch (Tirrul et al., 1983). At present, the Sistan Suture Zone exposes a well-preserved subduction zone complex, and preserves evidence for the closure of the Central Iranian Lut block against the Helmand block in the Middle or Late Eocene (Tirrul et al., 1983; Zarrinkoub et al., 2012).

The Sistan Suture Zone is characterized by a complex imbrication of thrust sheets, with rocks of various origins, variably deformed and metamorphosed. Mafic and ultramafic rocks and radiolarites represent remnants of the lithosphere of the Sistan oceanic basin and its pelagic sedimentary cover (Bonnet et al., 2018; Camp and Griffis, 1982). Ophiolites are present in both the Neh and the Ratuk Complexes (Fig. 1a–b). Coniacian ages of about 85 Ma date high pressure metamorphism (Bröcker et al., 2013) during (probably east-vergent)

subduction of the Sistan lithosphere. This was accompanied by deposition of a thick series of Late Cretaceous to Eocene flysch, considered to represent a fore-arc setting (e.g., Tirrul et al., 1983).

The Ratuk Complex is an accretionary prisms (Tirrul et al., 1983) flanked by the ophiolites and ophiolitic mélanges (Bonnet et al., 2018; Zarrinkoub et al., 2012). Thick flysch sequences of marine sedimentary turbidites are present in the Neh Complex and overlying Sefidabeh basin (Burg, 2018; Tirrul et al., 1983). There is a transition from slightly metamorphosed Paleocene flysch deposits to unmetamorphosed Eocene deposits and molasses-type sediments, indicating that collision probably started during the Eocene.

Adakitic granodiorites and A-type granites in the Ratuk Complex were emplaced in the Late Cretaceous and Early Eocene, respectively (Jentzer et al., 2020; Pang et al., 2013). These events were followed by widespread Eocene–Oligocene calc-alkaline volcanic activity.

Alkali basalts erupted along this complex and the Nayband fault from the Middle Miocene to the Quaternary (Pang et al., 2012).

2.2. The Neh Complex

The Neh Complex comprises a low-grade flysch-type metasedimentary assemblage with Late Cretaceous ophiolites, Late Cretaceous to Eocene phyllites, and Paleocene to Miocene terrigenous marine sedimentary rocks. These rocks host numerous granitoid plutons elongated in a NW-SE direction, including the Lakhshak pluton and related dykes, which are the subject of this paper (Fig. 1b–c).

Ophiolites constitute about 30% of the Neh Complex. Almost all of them face E-NE, as indicated by the overall stratigraphic polarity, pillowed tops, and the dip of layered gabbros, diabase dykes, and pelagic sedimentary rocks. Both upper and lower contacts are invariably steeply dipping faults, often marked by sheared serpentinite. Basalt is generally
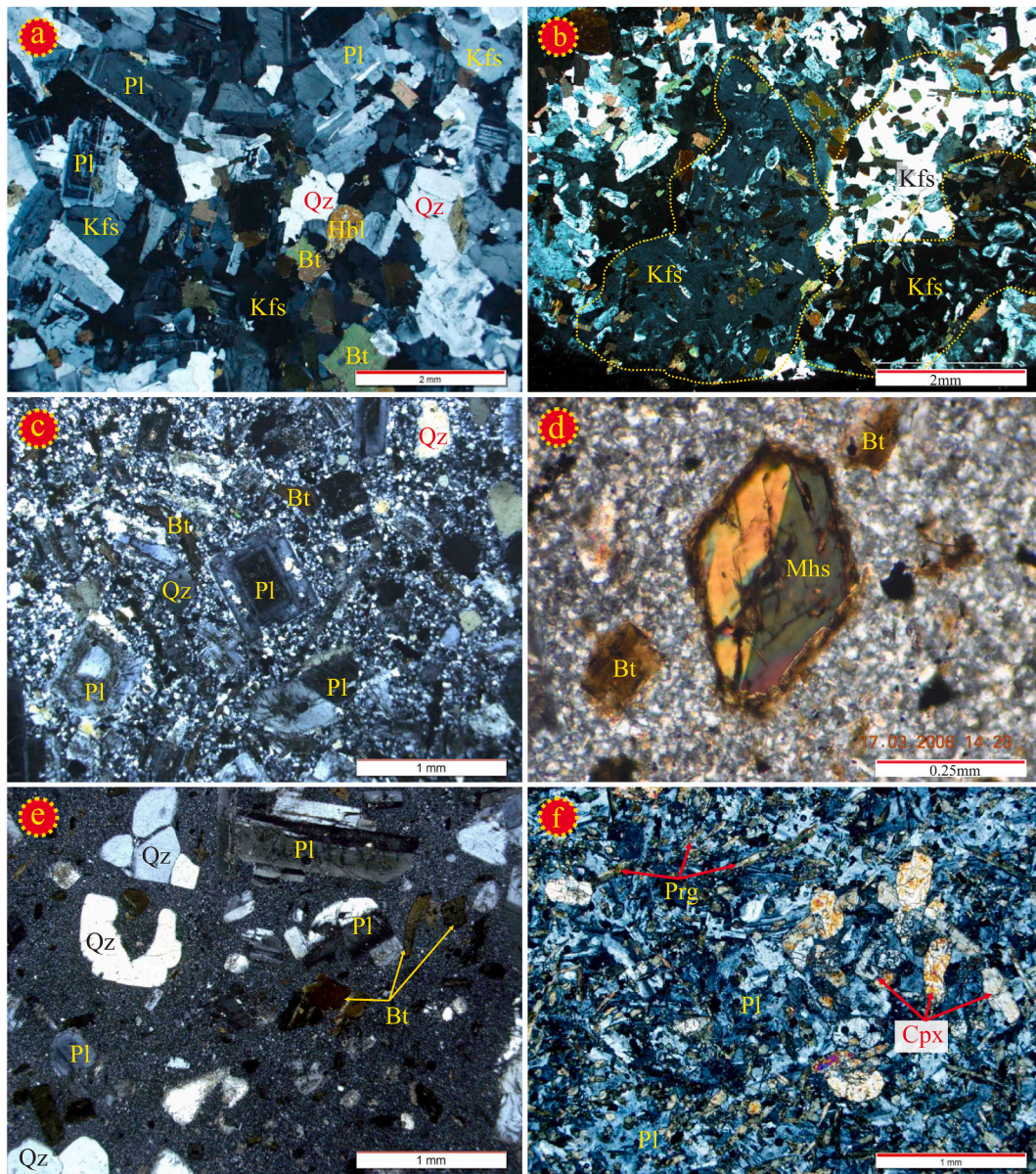
Fig. 3. Photomicrographs (in cross-polarized light). (a) Lakhshak granodiorite. (b) Lakhshak microgranular enclave with megacrysts of K-feldspar and poikilitic texture. (c), (d) and (e) Felsic (granodiorite / dacite) dykes. Plagioclase is euhedral with sieve texture. Magnesio-hastingsite is rimmed by biotite. Quartz is often partly resorbed and with rounded embayments. (f) Monzodiorite dyke with clinopyroxene, plagioclase and pargasite. Abbreviations are: Kfs = K-feldspar, Pl = plagioclase, Bt = biotite, Qz = quartz, Cpx = clinopyroxene, Hbl = hornblende, Prg = pargasite, Mhs = magnesio-hastingsite.

pillowed, with significant inter-pillow hyaloclastite and is typically overlain by, and locally interbedded with radiolarian chert and pelagic limestone, demonstrating eruption above the carbonate compensation surface. The sedimentary succession resting on the flows contains microfauna from the Late Turonian to Maastrichtian (Tirrul et al., 1983).

Phyllite constitutes about half of the Neh Complex surface outcrop (Fig. 1b–c). It occurs in weakly metamorphosed turbidite successions typically cropping out in long ridges bounded on the southwest and northeast by steeply dipping faults. Frequent reversals in facing and the presence of preserved fold hinges indicate many tight folds in addition to innumerable shear surfaces. Both bedding and shear surfaces have a dominant E-NE dip.

The flysch sequence was deposited in Late Cretaceous to Middle Eocene times based on stratigraphic and paleontological constraints (e. g., Nummulites aturicus, Discocyclina, Nummulites; Berberian, 1983; Burg, 2018; Bagheri and Gol, 2020). It dips ~75° to the NE and is overlain with an angular unconformity by Oligocene marl, sandstone

and basalt.

The Zahedan - Saravan granitoid plutons consist of several intrusions (Lakhshak, Gapdan, Zargoli, Pircha and South Zahedan; Fig. 1b–c). Rezaei-Kahkhaei et al. (2021) combined thermobarometry, geochronology, and lithological observations to document multi-stage emplacement of the Gapdan zoned pluton between 44 and 42 Ma, during progressive deformation and concurrent exhumation from a depth of ~5.0 km to ~2.5 km.

2.3. Regional structures

Three phases of deformation affected the marine sediments of the Neh Complex and Sefidabeh basin (Tirrul et al., 1983). The first two occurred between the Early Eocene and the Early Miocene. The oldest phase produced tight to isoclinal folds with an approximate easterly trend caused by the northward subduction of Sistan ocean floor under the Lut- Helmand blocks (Bagheri and Gol, 2020). The second, more

Table 1
Major (wt%) and trace element (ppm) abundances in the samples of Lakhshak pluton and dykes.

	Dyke				Pluton					
Rock type	Monzodiorite		Monzonite	Dacite	Granodiorite					
Sample NO	K-47	K-7	Z-R-7	Z-R-27	Z-R-73	K-27	K-44	K-50	F	Z-R-2
SiO_2	49.1	53.2	55.6	66.1	64.4	66	66.4	66.6	67.4	69.1
TiO_2	1.35	1.08	1.12	0.55	0.56	0.57	0.51	0.52	0.44	0.42
Al_2O_3	17.15	14.95	15.72	16.25	16.65	16.2	16.3	16.2	15.95	15.5
Fe_2O_3	8.17	7.28	6.89	3.56	3.82	3.51	3.28	3.34	3.04	2.63
MnO	0.12	0.12	0.11	0.06	0.07	0.06	0.06	0.06	0.06	0.05
MgO	5.19	6.9	4.72	1.67	2.02	1.65	1.6	1.5	1.52	1
CaO	8.83	7.4	6.66	3.82	4.12	3.77	3.62	3.66	3.37	2.73
Na_2O	3.69	3.35	3.61	4.18	4.37	4.16	4.54	4.37	4.28	4.08
K2O	3.32	2.21	3.31	2.62	2.74	2.74	2.59	2.77	2.94	3.3
Cr_2O_3	0.01	0.04	0.02	0.01	0.01	0.01	0.01	0.01	0.01	0.01
P_2O_5	0.76	0.38	0.54	0.18	0.21	0.19	0.15	0.18	0.15	0.14
Total	97.69	96.91	98.3	99	98.97	98.86	99.06	99.21	99.16	98.96
BaO	0.22	0.13	0.17	0.09	0.13	0.09	0.07	0.09	0.11	0.1
Ba	1935	1105	1440	727	1060	755	601	731	901	842
Rb	95	52.4	93.5	92.9	90.8	100	111.5	101	95.9	127.5
Sr	1385	641	804	547	696	527	472	442	527	571
Zr	186	143	164	160	160	153	164	150.5	140.5	145.5
Nb	23	15	19	11	11	13	12	11	10	12
Cr	80	330	150	30	40	30	30	30	30	10
La	62.9	37.3	52.4	36	39.1	35.1	27.5	25.3	35.1	36.2
Ce	118.5	68.8	92	63.3	69.8	64.7	52.5	49.2	62.2	65.4
Pr	12.7	7.3	9.2	6.1	6.8	6.6	5.5	5.1	6.1	6.5
Nd	48.4	27	34	21.3	24.1	24.3	19.6	19	21.5	22.5
Sm	8.8	5.1	6	3.5	4	4.3	3.7	3.5	3.6	3.7
Eu	2.3	1.4	1.6	0.9	1	1.1	0.9	0.9	0.9	0.9
Gd	7.7	4.8	5.7	3.2	3.8	3.9	3.2	3.2	3.5	3.3
Tb	0.9	0.6	0.7	0.4	0.4	0.5	0.4	0.4	0.4	0.3
Dy	4.6	3.3	3.6	1.9	2.3	2.6	2.2	2	2.1	1.8
Ho	0.9	0.6	0.7	0.3	0.4	0.5	0.4	0.4	0.4	0.3
Er	2.4	1.7	1.9	1.1	1.2	1.3	1.2	1.1	1.1	0.8
Tm	0.3	0.2	0.2	0.1	0.1	0.1	0.1	0.1	0.1	0.1
Yb	2	1.5	1.6	1	1	1.2	1	1	1	0.8
Lu	0.3	0.2	0.2	0.1	0.1	0.1	0.1	0.1	0.1	0.1
Y	26.1	18.2	20.5	11.6	13.4	14.8	12.8	11.8	12	10.1
Cs	2.1	1.4	3.8	3.3	3.4	3.1	5.2	4.7	3.4	4.5
Ta	1.2	0.9	1.2	1	0.9	1.1	1	1	0.9	1.1
Hf	5	4	4	4	4	4	5	4	4	4
Ga	21	19	18	19	19	19	21	20	18	19
Th	14	9	14	14	13	14	14	13	16	15
U	3.3	2.4	4.2	1.8	2.4	1.8	2.7	2.4	2.7	2.2
V	274	189	178	68	75	70	63	62	57	44
Co	48.8	48.4	37.9	90.9	60.4	71.5	59.5	58.5	59.7	76.3
Cu	54	90	33	5	13	6	5	10	7	5
Mo	1.34	1.34	1.34	1.34	1.34	1.34	1.34	1.34	1.34	1.34
Ni	51	92	46	15	24	14	16	13	18	7
Pb	13	6	7	18	19	19	18	20	17	21
Tl	0.34	0.34	0.34	0.34	0.34	0.34	0.34	0.34	0.34	0.34
Zn	88	74	55	65	65	67	68	65	56	58
Total REE	273	160	210	139	154	146	118	111	138	143
Eu*/Eu	0.85	0.87	0.84	0.82	0.78	0.82	0.8	0.82	0.78	0.79
ASI	0.67	0.7	0.73	0.98	0.94	0.97	0.97	0.96	0.98	1.02
Sr/Y	53.1	35.2	39.2	47.2	51.9	35.6	36.9	37.5	43.9	56.5
La/Yb	31.5	24.9	32.8	36	39.1	29.3	27.5	25.3	35.1	45.3
(La/Yb)N	21.2	16.76	22.08	24.27	26.36	19.72	18.54	17.06	23.66	30.51
Th/U	4.2	3.8	3.3	7.8	5.4	7.8	5.2	5.4	5.9	6.8
Th/Ba	0.01	0.01	0.01	0.02	0.01	0.02	0.02	0.02	0.02	0.02
Rb/Ba	0.05	0.05	0.06	0.13	0.09	0.13	0.19	0.14	0.11	0.15
Cr/Ni	1.57	3.59	3.26	2	1.67	2.14	1.88	2.31	1.67	1.43
liquidus T (°C)	1100	1057	1079	1055	1064	1049	1054	1056	1050	1023

dominant phase, associated with regional metamorphism, formed conjugate strike-slip faults and related upright, moderate to steep N-plunging folds. An associated pervasive cleavage trending N to NW developed in the Eocene turbiditic sediments of the Sefidabeh basin and the ophiolitic mélange (Bagheri and Gol, 2020; Tirrul et al., 1983). This phase of deformation corresponds to an E-NE direction of maximum horizontal shortening. The third phase of deformation formed large strike-slip faults and folding in the Pliocene-Quaternary and accompanied recent volcanism. There are two systems of N-NE trending right-lateral strike-slip faults and W-NW-trending left-lateral strike-slip faults.

3. The Lakhshak pluton

3.1. General features

The Lakhshak pluton has an ellipsoidal outcrop, a surface area of approximately 87 km², and is intruded into low-grade Eocene schists (Figs. 1c and 2a–b). The pluton has no foliation, with the exception of the SW border, which has a subvertical planar-linear fabric parallel to the contact. The local deformation is synkinematic and characterized regionally by NW oriented dextral shear zones. The intrusion caused

Table 2
Representative composition of pyroxene in monzodiorite dyke K-47. Temperature and pressure calculated based on Putirka et al. (2003).

| Location	Core	Near core	Boundary core - rim	Rim	Core	Core
SiO$_2$	51.35	50.05	49.37	47.85	49.42	51.21
TiO$_2$	0.79	1.12	1.23	1.65	1.13	0.64
Al$_2$O$_3$	3.5	4.83	5.48	6.28	5.31	3.32
FeO	5.47	6.16	6.35	6.67	6.12	6.26
Cr$_2$O$_3$	0.22	0.06	0.09	0.15	0.04	0.04
MnO	0.17	0.18	0.16	0.18	0.11	0.14
MgO	15.61	15.23	14.49	13.78	14.78	15.44
CaO	21.86	21.26	22.3	23.14	22.5	22.1
Na$_2$O	0.4	0.47	0.43	0.35	0.43	0.41
K$_2$O	0.02	0.01	0	0.02	0	0.02
Total	99.39	99.37	99.91	100.09	99.84	99.58

contact metamorphism converting slates and phyllites to biotite or actinolite schist and rarely garnet biotite schist near the margin of the pluton. The foliation of the country rocks, defined mainly by biotite ± sericite or crenulation cleavage, is well-developed and trends NW.

Mafic microgranular enclaves are widespread in the pluton. They are mostly elliptical or oval in shape and range from a few to <10 cm in size (Fig. 2c). The contacts between the enclaves and the host rocks are sharp or transitional.

3.2. Mineralogy and textures

Over 250 samples were collected from the Lakhshak pluton and the related dykes. The modal mineralogy of 23 samples was determined by point counting with a Swift automatic counter fitted to a polarizing microscope. On each thin-section a total of 1500–2200 points were counted, and then normalized to 100% for the rock classification. The results show that the pluton is medium-grained, mesocratic, with a typical holocrystalline and granular texture. It is composed of plagioclase (47%), hornblende (7%), quartz (19%), K-feldspar (14%), biotite (11%) and accessory zircon, apatite, titanite and allanite (<2%; Fig. 3a). Based on the quartz–alkali feldspar–plagioclase modal classification, the pluton is granodioritic. Except for a decrease of the hornblende content from the center to the margin, the pluton has a homogeneous mineral composition and an isotropic fabric.

Plagioclase occurs as euhedral to subhedral crystals, ~1–1.5 mm in
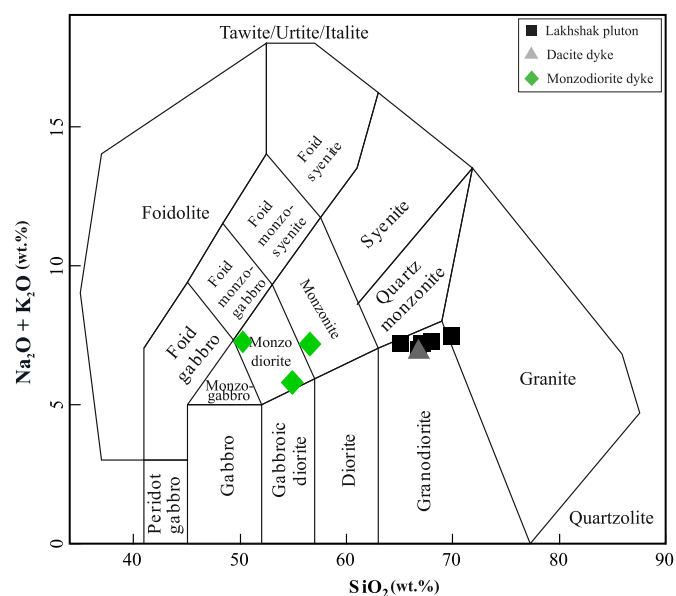
Fig. 4. TAS the diagram of Middlemost (1994) with data for the Lakhshak pluton and dykes.

size, showing generally a complex oscillatory zoning (Fig. 3a). It locally contains apatite and zircon, and is rarely altered to secondary minerals (e.g., calcite, epidote). *K-feldspar* is subhedral, fresh, and ~ 1 mm in size. In deformed rocks, it also shows flame perthite and microcline textures. The local stress concentrations were sufficient to promote the nucleation of flame perthite. Cross-hatching of microcline forms by intersecting sets of albite and pericline twin lamellae due to the transformation from monoclinic to triclinic symmetry. In the mylonitic rocks at the SW margin of the pluton, K-feldspar is partly replaced by myrmekite, which developed through plagioclase and quartz intergrowth during high temperature solid state. *Quartz* has anhedral shapes and forms isolated interstitial pockets, which appear to have crystallized later than the other minerals. It contains some apatite and in the deformed rocks at the SW margin it shows myrmekite and ribbon textures. *Biotite* occurs generally as subhedral to euhedral crystals with inclusions of apatite needles and minor zircons. *Hornblende* is euhedral to subhedral and locally intergrown with biotite.

The mafic microgranular enclaves are dioritic to quartz monzonite in composition and show textures varying from equigranular to porphyritic, indicative of an igneous origin (Vernon, 1984). Some K-feldspars in enclaves appear as megacrysts with poikilitic texture and contain many inclusions of small crystals of plagioclase and biotite (Fig. 3b).

3.3. Dykes

The pluton is cut by numerous NE striking dykes that locally occupy 20 to 30% of its volume (Fig. 2a–b). The dykes generally do not show chilled margins. They can be divided on the basis of petrography and norm into two groups of felsic and intermediate to basic dykes.

3.3.1. Felsic dykes

Felsic dykes are quite abundant by volume, but heterogeneously distributed and from <1 m to about 12 m thick. They are dacitic / granodioritic in composition and display porphyritic textures (with variable microcrystalline groundmass) and in part glomeroporphyritic textures with phenocrysts of quartz and plagioclase (Fig. 3c–e). The mineral assemblage consists dominantly of plagioclase, biotite, resorbed quartz with/without green-brown hornblende phenocrysts, with subordinate opaque minerals (2–4%), apatite (<1%), allanite and pyrite (few grains). In few places, when the thickness of dykes exceeds 2 m, they display a good shape preferred orientation, marked by plagioclase phenocrysts. The groundmass consists of tiny quartz and K-feldspar (Fig. 3c–e).

Plagioclase is euhedral and locally displays signs of disequilibrium rims, along with sieve textures, melt and/or mineral inclusions (apatite and zircon), and optical zoning (Fig. 3c). *Biotite* is euhedral and partially altered to chlorite. *Hornblende* is euhedral to subhedral, with well developed zonation seen in plan polarized light, and rimmed by a thin layer of biotite, suggesting disequilibrium with their host melt or destabilization during magma ascent (Fig. 3d). *Quartz* is often partly resorbed and with rounded embayments (Fig. 3e). Embayed phenocrysts also suggest disequilibrium with the host magma, perhaps reflecting magma mixing.

3.3.2. Intermediate to basic dykes

Intermediate to basic dykes are monzonite and monzodiorite in compositions. These dykes are <1 m thick and are less common in the study area. They often have a microgranular texture. *Plagioclase* and zoned *amphibole* are the predominant phases, and their size usually ranges from 0.1 to 1 mm (Fig. 3f). Euhedral amphibole is fresh, brown and pleochroic. Few anhedral *quartz* grains have been observed, surrounded by fine grain hornblendes. *Pyroxenes* are uncommon, small and generally <10% in abundance.
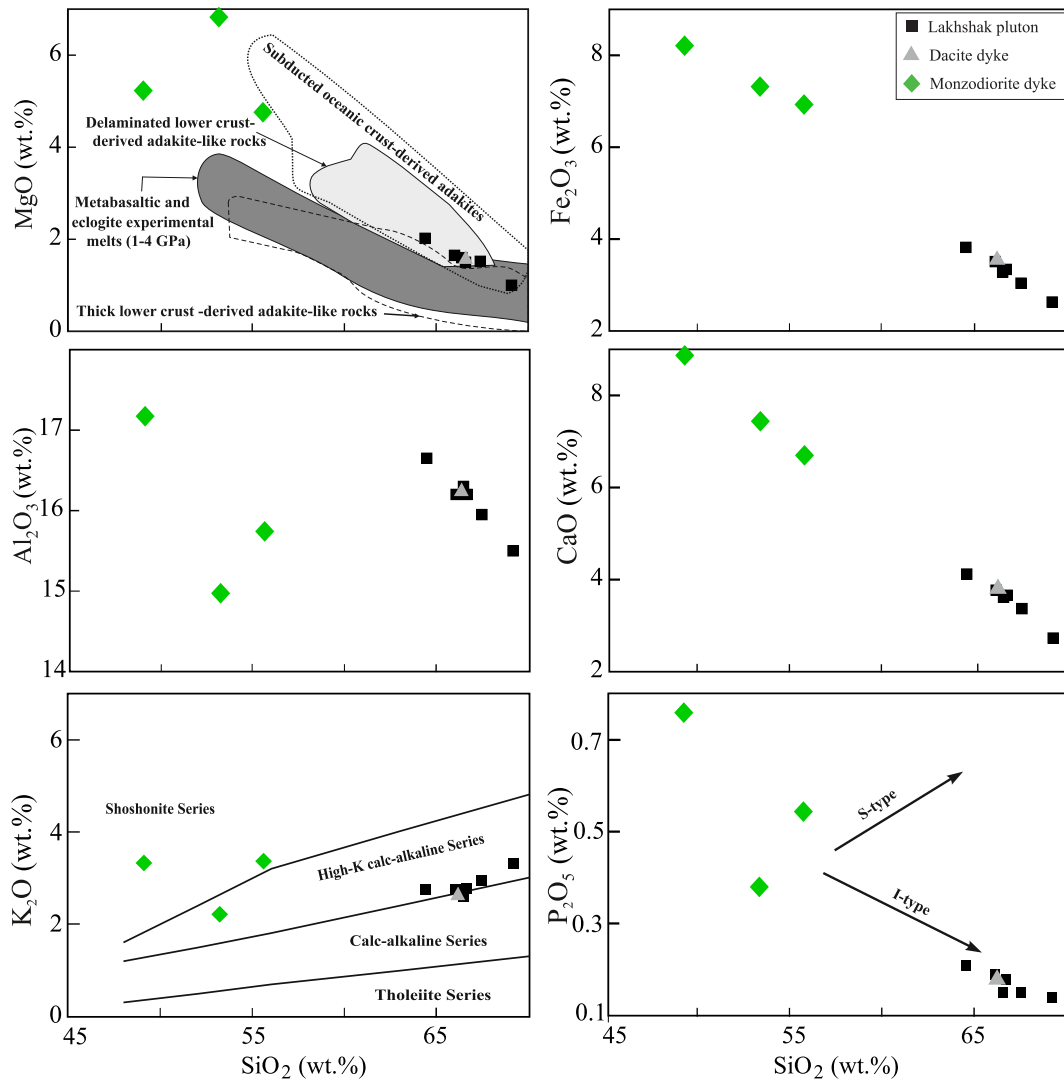
Fig. 5. Selected major oxides vs. SiO_2 (wt%) contents for the Lakhshak pluton and related dykes. In the MgO vs. SiO_2 diagram the Lakhshak pluton and dacite dykes plot in the field of subducted oceanic crust-derived adakites (modified after Wang et al., 2016). The plot of K_2O vs. SiO_2 shows the high-K calc-alkaline nature of the study rocks (modified after Peccerillo and Taylor, 1976). The I and S-type arrays in the plot of P_2O_5 vs. SiO_2 are after He et al. (2018).

4. Analytical methods

4.1. Whole-rock chemistry

After the macroscopic and microscopic investigation, ten samples were analyzed for major and trace elements after fusion of 0.2 g of rock powder with 1.5 g $LiBO_2$ and dissolution in 100 ml 5% HNO_3 at ALS Chemex Company in Canada. Loss on ignition was determined by drying the samples at 1000 °C. Rare earth element (REE) analyses were performed by Inductively Coupled Plasma–Mass Spectrometry (ICP-MS). Detection limits are 0.01–0.1 wt% for major oxides, 0.1–10 ppm for trace elements, and 0.01–0.5 ppm for REEs. Chemical analyses of representative samples from the Lakhshak pluton and the dykes are given in Table 1.

4.2. Mineral chemistry

Four samples were prepared for electron microprobe analyses, including two from the Lakhshak pluton (Z-R-13 and K-13), one from a dacite dyke (Z-R-27) and one from a monzodiorite dyke (K-47). The in situ analyses were carried out at the Department of Geosciences, University of Oslo (Norway), using a CAMECA SX100 electron microprobe

equipped with four WDS and one EDS. The operating conditions were as follows: 15 kV accelerating voltage, 15 nA beam current and 10 s counting time on peak position. Detection limits are 0.2–0.6 wt%. The cation numbers of the feldspar, biotite and amphibole were calculated by Minpet 2.02 software based on 8, 22 and 23 oxygens, respectively (Tables 2–4).

4.3. Sr-Nd isotopes

Isotope analyses of Sr and Nd were carried out at Universidad Complutense, Madrid (Spain), using standard separation and mass-spectrometric techniques and a VG Sector 54 instrument. The Rb, Sr, Sm and Nd concentrations were obtained by X-ray fluorescence spectrometry at the X-Ray Diffraction Centre of the Complutense University. Samarium and Nd were analyzed by isotope dilution using spikes enriched in ^{149}Sm and ^{150}Nd. The decay constants used in the calculations are: $\lambda^{87}Rb = 1.42 \times 10^{-11}$ and $\lambda^{147}Sm = 6.54 \times 10^{-12}$ y^{-1}. The Sr analyses were corrected for possible ^{87}Rb interferences and $^{87}Sr/^{86}Sr$ was normalized to the reference value $^{88}Sr/^{86}Sr = 0.1194$. The Nd analyses were corrected for possible ^{142}Ce and ^{147}Sm interferences and normalized to $^{146}Nd/^{144}Nd = 0.7219$. Replicate analyses of NBS 987 yielded an average $^{87}Sr/^{86}Sr = 0.710203 \pm 0.00004$ (2σ; $n = 10$).
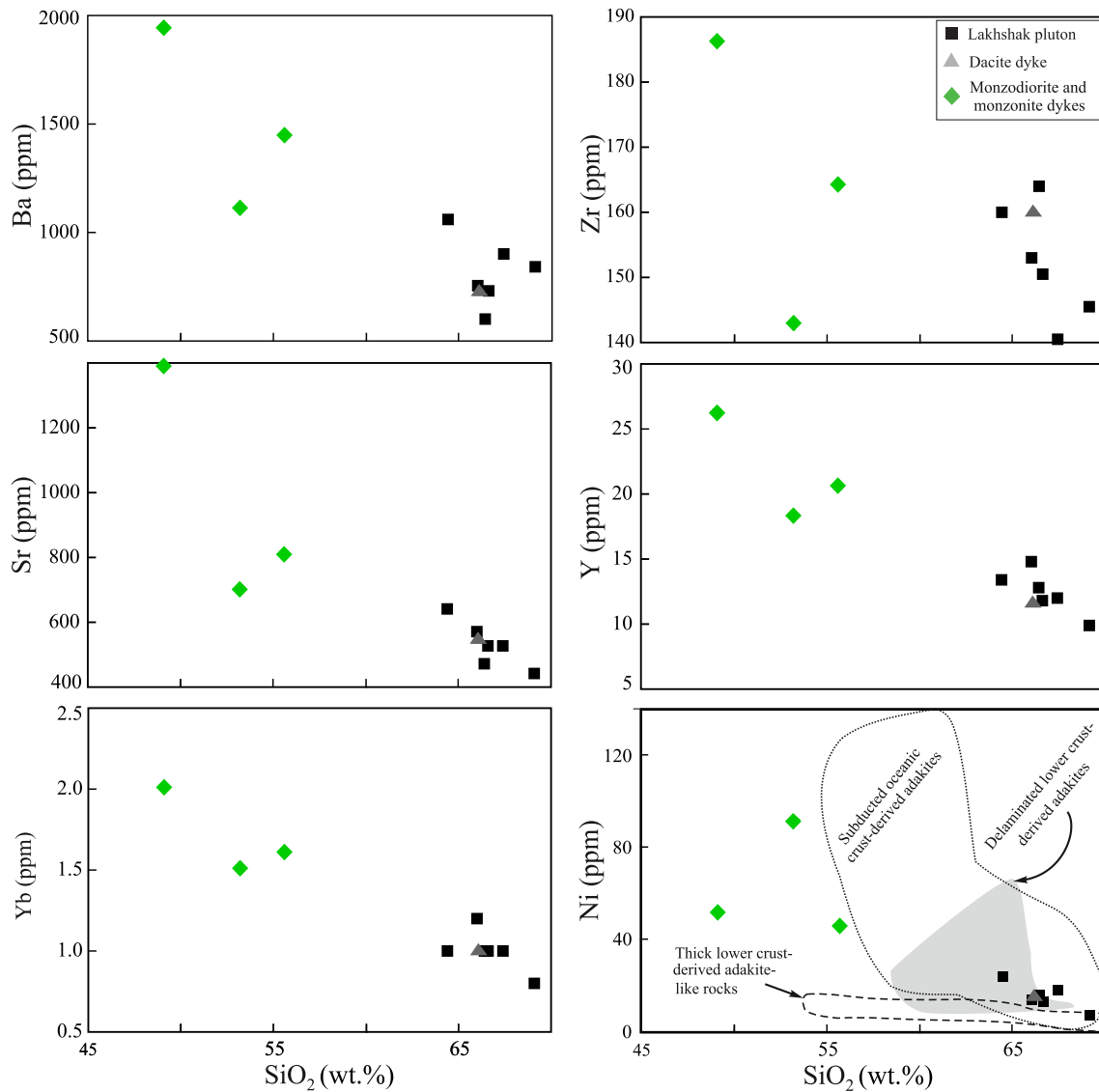
Fig. 6. Selected trace element (ppm) vs. SiO₂ (wt%) contents for the Lakhshak pluton and related dykes. The Ni vs. SiO₂ diagram distinguishes different types of adakites based on their origins (modified after Wang et al., 2016). The Lakhshak samples plot in the field of subducted oceanic crust-derived adakites.

Analyses of La Jolla yielded an average $^{143}Nd/^{144}Nd = 0.511844 \pm 0.00002$ (2σ; n = 7). Analytical uncertainties are estimated to be ±1% for $^{87}Rb/^{86}Sr$, 0.01% for $^{87}Sr/^{86}Sr$, 0.1% for $^{147}Sm/^{144}Nd$ and 0.006% for $^{143}Nd/^{144}Nd$. Results are reported in Table 5.

4.4. U-Pb isotopes

The U-Pb analyses were carried out with the ID-TIMS technique at the University of Oslo. Rock samples were crushed in a jaw crusher and pulverized with a Retsch mill model SK100. The heavy mineral fractions were separated by a combination of Wilfley table, magnetic separation and heavy liquid (methylene iodide) flotation. The analyzed minerals were selected under a binocular microscope. Zircon was chemically abraded (Mattinson, 2005), except for some high-U samples; the latter and titanite were air abraded. Zircon, titanite, feldspar and hornblende were dissolved in HF(+HNO₃) after addition of a mixed ^{202}Pb-^{205}Pb-^{235}U spike, followed by HCl, with subsequent purification of Pb and U in anion exchange resin with HCl or HBr + HNO₃ procedures (Corfu, 2004). Lead and U were analyzed with a MAT 262 mass spectrometer with Faraday cups in static mode, or for small amounts of Pb and U and for all $^{207}Pb/^{204}Pb$ ratios using an ion-counting secondary

electron multiplier (Tables 6 and 7). Fractionation of Pb was corrected using the $^{202}Pb/^{205}Pb$ ratio of the spike and in accordance with daily measurements of NBS 982-Pb and U-500 standards. Blank corrections were ≤ 2 pg for Pb and 0.1 pg for U. The uncertainties are given at 2σ and integrate the main error contributions. The initial Pb correction was done using Stacey and Kramers (1975) values, except for titanite where coexisting feldspar and amphibole were used for the initial Pb (Table 7). Decay constants are those of Jaffey et al. (1971). The ages were calculated and the data plotted using the program Isoplot/Ex Version 3.75 (Ludwig, 2003). A correction was also made for the deficit in ^{206}Pb caused by ^{230}Th disequilibrium (Schärer, 1984) deriving Th/U$_{magma}$ from the whole rock compositions of the corresponding units (Table 6).

5. Results

5.1. Major and trace elements

The SiO₂ content of the pluton samples ranges from 64.4 to 69.1 wt %, and for the dyke samples from 49.1 to 66.1 wt% (Table 1). In the TAS diagram of Middlemost (1994); Fig. 4), the pluton samples and the felsic dykes plot in the granodiorite field (except for sample Z-R-2, collected
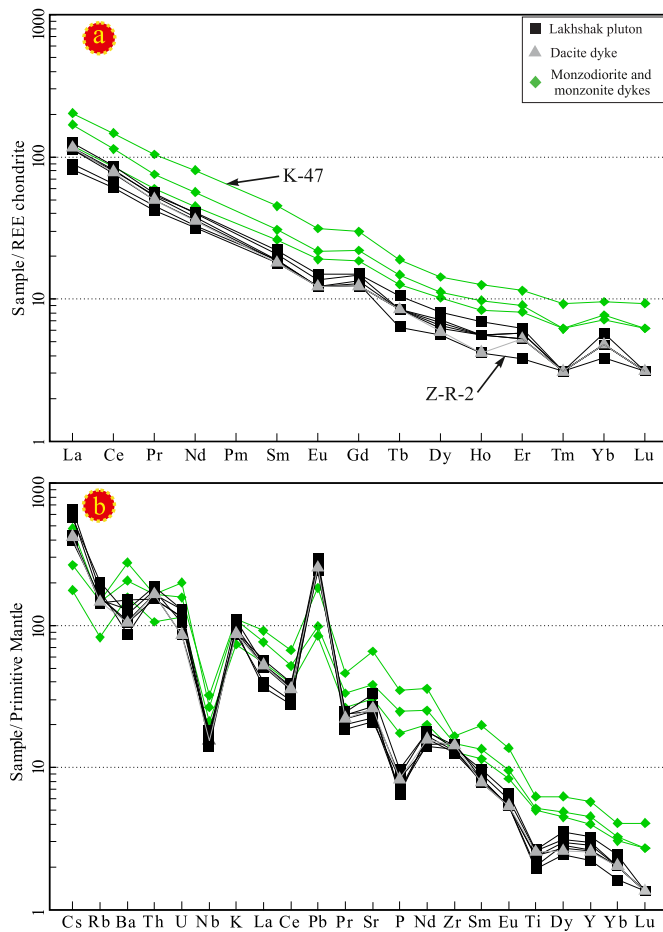
Fig. 7. (a) Chondrite-normalized rare earth element plot for the Lakhshak pluton and related dykes. (b) Primitive mantle normalized trace element patterns. Normalization values after Boynton (1984), and Sun and McDonough (1989), respectively.

from the pluton margin, that plots at the margin of the granite field). The intermediate-basic dyke samples correspond to monzodiorite to monzonite according to the quartz–alkali feldspar–plagioclase classification.

The aluminium saturation index, ASI [molar $Al_2O_3/(CaO + Na_2O + K_2O)$], is nearly constant (0.94–1.02) for rocks of the pluton (Table 1), but increases with SiO_2 from 0.67 to 0.98 for the dykes. The rocks are high-K calc-alkaline, apart from samples K-47 (a monzodiorite dyke) and *Z-R-7* (a monzonite dyke), which plot in the field of the shoshonite series (Fig. 5).

The Lakhshak granodiorites and the dykes are Na-rich (Na_2O = 3.35–4.54; Na_2O/K_2O = 1.1–1.8) and have relatively high Al_2O_3 (14.95–17.15 wt%) and MgO (1.00–6.90 wt%) (Table 1). In addition, they have high Sr (442–1385 ppm), Ni (7–92 ppm) and Cr (10–330 ppm) contents and low Yb (0.8–2 ppm) and Y (10.1–26.1 ppm), and Eu/Eu* = 0.78–0.89 (Table 1). These geochemical characteristics are comparable to those of adakites (SiO_2 > 56 wt%, Al_2O_3 > 15 wt%, Na_2O > 3.5 wt%, Na_2O > K_2O, relatively high Ni (≥20 ppm), Cr (30–40 ppm) and Eu/Eu* ~ 1) as reported by Defant and Drummond (1990), Drummond and Defant (1990), Richards and Kerrich (2007) and Castillo (2012). The ratios of Sr/Y (35–57) and La/Yb (25–45) (Table 1) are within the range of those in typical adakites (Sr/Y > 20 and La/Yb >20; Castillo, 2012).

On Harker variation diagrams, the pluton and dykes mostly show common trends of decreasing MgO, Fe_2O_3, CaO, MnO, TiO_2, Ba, Zr, Sr, Y and Yb with increasing SiO_2 (Figs. 5 and 6).

The Lakhshak granodiorites and dykes have relatively high total REE abundances (111–273 ppm; Table 1), highest in the monzodiorite dykes

and lowest in the granodiorites. In a chondrite-normalized REE plot they exhibit parallel patterns with high LREE/HREE ratios [$(La/Yb)_N$ = 17–31] (Table 1; Fig. 7a). All the samples are enriched in large-ion lithophile elements (LILE, such as Rb, Ba, Sr) and LREE, and depleted in high-field strength elements (HFSE, such as Nb, Ta, Ti) (Fig. 7b). The remarkable P depletion in the Lakhshak granodiorites could be the result of apatite fractionation.

5.2. Mineral chemistry

Feldspar, amphibole and pyroxene compositions in the Lakhshak pluton and related dykes are used to assess temperatures and pressures during magma evolution. The samples are: *Z*-R-13 and K-13 (from the center and margin of the Lakhshak pluton, respectively); K-47 (a 2.5 m thick monzodiorite dyke, trending N30/80NW); and Z-R-27 (a 1 m thick dacite dyke, trending N117/85SW).

5.2.1. Pyroxene

Pyroxene is just present in monzodiorite dykes, especially in dykes with SiO_2 ~ 49 wt%. It occurs as microphenocrysts (0.03 to 0.5 mm in size), which are locally zoned with cores low in Fe and Ca and rims with more Fe and Ca, while MgO is higher in the core than in the rim (sample K-47, Table 2). Pyroxenes are classified as calcium pyroxenes, according to the QUAD diagram (Ca + Mg + Fe^{2+}) - J (2Na) of Morimoto (1988) and plotted in the Wo-En-Fs diagram (wollastonite - enstatite - ferrosilite) they are predominantly diopside, both in the core and the rim of the crystals, ranging from $Wo_{45.56}En_{45.27}Fs_{9.18}$ to $Wo_{46.94}En_{42.91}Fs_{10.16}$ (Fig. 8a).

5.2.2. Feldspar

Feldspar occurs as medium-grained crystals. The plagioclase is mainly oligoclase to andesine in the Lakhshak pluton and the dacite dykes whereas the monzodiorite dykes contain a slightly more calcic plagioclase with An up to 50% (labradorite) (Table 3, Fig. 8b). Plagioclase is zoned, especially in dacite dykes where it shows the best developed oscillatory zoning with several thin layers, and with CaO decreasing from the core to the core-rim boundary, and then increasing again to the outer rim (Table 3; Fig. 3c).

The Or content of K-feldspar ranges from 83 to 87% % in the Lakhshak granodiorite and 90 to 92% in the monzodiorite dyke.
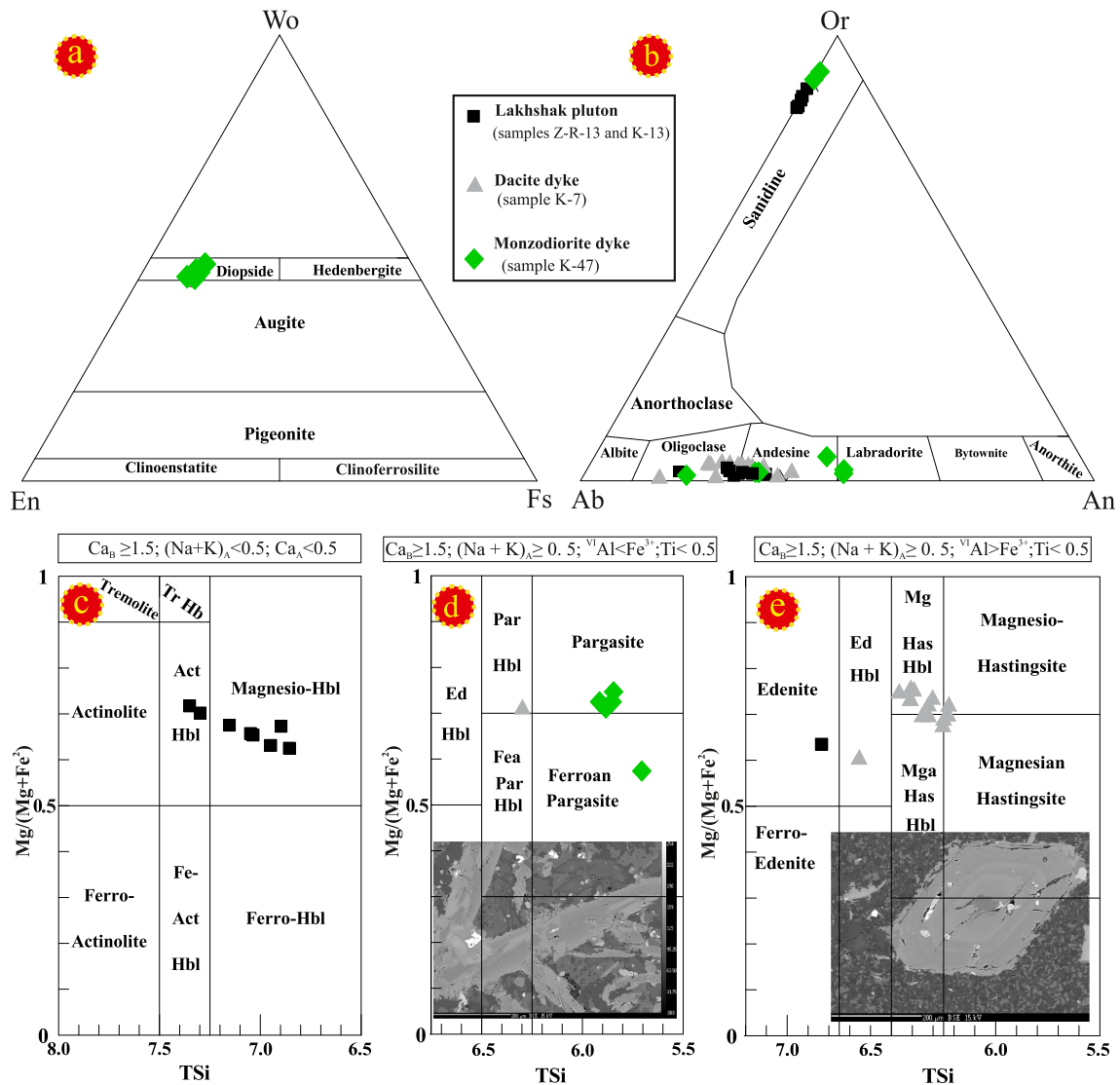
5.2.3. Amphibole

Amphibole is green in the Lakhshak pluton and the dacite dykes and brown in the monzodiorite dykes. In any given sample, amphibole crystals, regardless of size, display a narrow chemical composition. They are all members of the calcic amphiboles, although there are obvious differences between them: often magnesio- hornblende and rarely edenite in the pluton (Fig. 8c), pargasite in the monzodiorite dykes (Table 4, Fig. 8d), and magnesio-hastingsite, pargasite and edenite in the dacite dykes (Fig. 8e). Suhedral and prismatic pargasite in the monzodiorite dykes show different responses in BSE images (Fig. 8d).

Amphibole in the dacite dykes has a well developed zoning and its composition changes from core to rim in several ways, from magnesio-hornblende to pargasite, pargasite to magnesio-hornblende or edenite to magnesio-hornblende (Table 4). They have been tentatively correlated by combining BSE images with electron microprobe analyses (Fig. 8e).

5.3. Sr-Nd isotopes

Six whole-rock samples were analyzed for the Sr and Nd isotope composition: three from the Lakhshak pluton (*Z*-R-1, Z-R-2 and Z-R-22), one from a dacite dyke (Z-R-9), one from a monzodiorite dyke (Z-R-16), and one from the country rocks, green schist (Z-SH). The initial $^{87}Sr/^{86}Sr$ and $^{143}Nd/^{144}Nd$ ratios were calculated based on the U-Pb ages (Table 5) but since age corrections are small, the ratios are insensitive to

Fig. 8. (a) Pyroxene compositions, plotted in the Wo-En-Fs diagram (Fabries et al., 1988), correspond to diopside. (b) Ternary classification diagram Ab-An-Or for feldspars (Jones, 1989). (c), (d) and (e) Variations of $Mg/(Mg + Fe^{2+})$ vs. Si (apfu) for the calcic amphiboles.

uncertainties in either age or Rb/Sr ratio. The initial $^{87}Sr/^{86}Sr$ ratios of granodiorites and dykes are relatively uniform at 0.7048–0.7058. The initial $^{143}Nd/^{144}Nd$ ranges from 0.5121 to 0.5128, corresponding mostly to initial ε_{Nd} values around 0 ± 2, except for a more negative value of -8.6 from one of the granodiorite samples.

5.4. U-Pb geochronology

Zircon and titanite in two granodiorite samples of the Lakhshak pluton and two dykes, were dated. Feldspar and green hornblende were also separated for measuring the common lead composition of the magma used to correct the initial Pb in titanite and also to obtain information on the source of the magmas (Table 6).

5.4.1. Lakhshak granodiorite sample Z-R-60

The sample selected for dating is a medium-grained granular granodiorite from the pluton margin (Fig. 1c). Zircons were mostly small, rectangular and very clear in transmitted light (Fig. 9a). Zircon fractions were selected based on morphology and their response to partial dissolution after chemical abrasion. They included long clean zircon (35 grains), long milky zircons (17 grains) and tips of zircons (22 tips; Fig. 9a). One analysis is discordant indicating the presence of an

inherited component. The two analyses of long milky prisms and tips of zircon overlap near the Concordia curve yielding a weighted average $^{206}Pb/^{238}U$ age of 29.90 ± 0.05 Ma. Two fractions of titanite of different sizes yield an indistinguishable average $^{206}Pb/^{238}U$ age of 29.86 ± 0.59 Ma (Fig. 9a). We propose that the combined zircons and titanites data define a robust age of 29.9 ± 0.1 Ma for the crystallization of the granodiorite (Fig. 9a).

5.4.2. Lakhshak granodiorite sample K-50

This was collected from near the pluton center and is also a medium-grained granular granodiorite with the same mineralogy as sample Z-R-60. The zircons were mostly small, rectangular and clear in transmitted light with different morphologies. All grains are between 70 and 250 μm in size with elongation (length-to-width) ratios ranging from 1 to 7. They also carry inclusions of other minerals such as apatite. After chemical abrasion, three fractions were picked for dating including long clean zircon (23 grains with elongation 5:1), long partially milky zircons (32 grains) and short partially milky zircons (30 grains) (Fig. 9b). They show a range of discordance and $^{206}Pb/^{238}U$ ages from 35.54 ± 0.09 to 29.98 ± 0.08 Ma (Table 6). The older zircon fractions are likely mixtures of magmatic and xenocrystic components, while the youngest defining an age of crystallization indistinguishable from that of sample Z-R-60.

Table 3

Representative compositions of feldspars in the Lakhshak pluton and related dykes. Abbreviation: Pl = Plagioclase; Kfs = K-feldspar; C1, 2, 3 = sequence from centre to margin of core; C-R = boundary core to rim; R1, 2, 3 = sequence from inner to outer rim.

Sample No			K- 47 (Monzodiorite dyke)			
Mineral	Pl 1		Pl 2	Pl 3	Kfs	Kfs
Location	C	R				
SiO$_2$	55.19	62.85	54.91	55.87	63.19	65.11
TiO$_2$	0.05	0.02	0.03	0.04	0.01	0.03
Al$_2$O3	27.72	22.46	27.73	27.03	18.3	18.4
FeO	0.64	0.32	0.69	0.53	0.15	0.18
MnO	0.02	0	0.02	0.02	0	0
CaO	10.36	4.4	10.48	9.37	0.14	0.07
Na$_2$O	5.47	9.48	5.51	5.64	0.83	1.09
K$_2$O	0.34	0.14	0.28	0.93	15.68	15.34
Total	99.79	99.66	99.64	99.44	98.31	100.23
Si	2.5	2.8	2.49	2.54	2.98	3
Al	1.48	1.18	1.48	1.45	1.02	1
Fe^{2+}	0.02	0.01	0.03	0.02	0.01	0.01
Ca	0.5	0.21	0.51	0.46	0.01	0
Na	0.48	0.82	0.49	0.5	0.08	0.1
K	0.02	0.01	0.02	0.05	0.94	0.9
Ab	47.9	79	48	49.4	7.4	9.7
An	50.1	20.3	50.4	45.3	0.7	0.3
Or	2	0.8	1.6	5.4	91.9	90

Sample No																				Z-R-27 (Dacite dyke)
Mineral	Pl 1						Pl 2							Pl 3					Pl 4		
Location	C1	C2	C3	C-R	R1	R2	C1	C2	C3	C-R	R1	R2	R3	C1	C2	C-R	R1	R2	C	C-R	R
SiO$_2$	61.69	60.94	59.81	59.43	60.76	64.85	59.6	60.33	59.65	60.21	59.83	59.16	61.24	62.25	61.36	58	59.42	58.31	61.54	58.33	59.32
TiO$_2$	0.03	0	0	0.03	0.04	0.02	0.01	0.01	0.01	0.02	0.01	0	0.01	0.02	0.01	0	0	0.03	0.01	0	0.02
Al$_2$O3	23.92	24.05	24.16	24.91	24.3	21.88	24.49	24.08	24.55	24.49	24.39	24.76	23.57	22.94	24.06	25.66	24.72	25.26	22.97	24.9	24.91
FeO	0.14	0.15	0.2	0.16	0.27	0.12	0.18	0.21	0.19	0.15	0.2	0.26	0.18	0.16	0.21	0.16	0.16	0.23	0.04	0.19	0.22
MnO	0	0.01	0.03	0.05	0.03	0	0	0	0	0	0	0.03	0.01	0.01	0.04	0.02	0	0	0	0	0.02
CaO	5.73	6.02	6.69	7.33	6.43	3.2	6.94	6.61	7.28	6.76	6.84	7.15	5.5	4.85	6.3	8.4	7.04	8.01	5.52	7.94	7.18
Na$_2$O	8.12	7.8	7.61	7.55	8.1	10.08	7.56	7.86	7.45	7.61	7.6	7.62	8.66	8.35	7.91	6.72	7.62	7.19	8.49	7.27	7.47
K$_2$O	0.65	0.56	0.55	0.48	0.39	0.19	0.34	0.55	0.51	0.5	0.47	0.32	0.15	0.7	0.61	0.42	0.34	0.25	0.69	0.34	0.27
Total	100.27	99.52	99.05	99.93	100.32	100.34	99.11	99.65	99.64	99.74	99.33	99.3	99.31	99.28	100.5	99.39	99.3	99.28	99.27	98.96	99.4
Si	2.74	2.73	2.7	2.66	2.7	2.85	2.68	2.7	2.68	2.69	2.69	2.67	2.74	2.78	2.72	2.62	2.67	2.63	2.76	2.64	2.67
Al	1.25	1.27	1.28	1.31	1.27	1.13	1.3	1.27	1.3	1.29	1.29	1.31	1.24	1.21	1.26	1.36	1.31	1.34	1.21	1.33	1.32
Fe^{2+}	0.01	0.01	0.01	0.01	0.01	0.01	0.01	0.01	0.01	0.01	0.01	0.01	0.01	0.01	0.01	0.01	0.01	0.01	0	0.01	0.01
Ca	0.27	0.29	0.32	0.35	0.31	0.15	0.34	0.32	0.35	0.32	0.33	0.35	0.26	0.23	0.3	0.41	0.34	0.39	0.27	0.39	0.35
Na	0.7	0.68	0.67	0.66	0.7	0.86	0.66	0.68	0.65	0.66	0.66	0.67	0.75	0.72	0.68	0.59	0.67	0.63	0.74	0.64	0.65
K	0.04	0.03	0.03	0.03	0.02	0.01	0.02	0.03	0.03	0.03	0.03	0.02	0.01	0.04	0.03	0.02	0.02	0.01	0.04	0.02	0.02
Ab	69.3	67.9	65.2	63.4	68	84.1	65.1	66.2	63.1	65.2	65.1	64.7	73.4	72.7	67.2	57.8	65	61	70.7	61.2	64.3
An	27	28.9	31.7	34	29.9	14.8	33	30.7	34.1	32	32.3	33.5	25.8	23.3	29.5	39.9	33.1	37.6	25.5	36.9	34.2
Or	3.7	3.2	3.1	2.6	2.1	1.1	1.9	3	2.8	2.9	2.6	1.7	0.8	4	3.4	2.4	1.9	1.4	3.8	1.8	1.5

Sample No	Z-R-13 (Lakhshak granodiorite)										K-13 (Lakhshak granodiorite)				
Mineral	Pl 1				Pl 2			Pl 3	Kfs	Kfs	Pl 1			Kfs	Kfs
Location	C	C-R	R1	R2	C	C-R	R	C			C	C-R	R		
SiO_2	60.29	59.39	61.34	59.92	58.6	59.65	60.87	60.12	63.52	64.19	61.07	61.26	63.54	64.75	64.92
TiO_2	0.02	0.02	0.01	0	0	0.02	0	0.02	0.0077	0.013	0	0	0	0	0.013
Al_2O_3	24.14	24.58	24.27	24.13	24.83	24.9	24.43	24.14	17.91	18.36	24.01	23.89	22.08	18.13	18.16
FeO	0.18	0.21	0.2	0.23	0.18	0.19	0.1	0.13	0.096	0.15	0.2	0.17	0.12	0.071	0.12
MnO	0.02	0.02	0	0	0.01	0	0	0.01	0.013	0.015	0	0	0.02	0.012	0
CaO	6.23	6.91	5.84	6.48	7.56	7.31	6.11	6.52	0.059	0.0033	6.19	5.77	3.89	0.033	0
Na_2O	7.88	7.69	8.07	7.73	7.49	7.56	8.03	7.96	1.74	1.54	8.08	8.24	9.51	1.63	1.37
K_2O	0.29	0.28	0.39	0.39	0.27	0.27	0.22	0.33	14.39	14.94	0.44	0.51	0.39	14.83	15.3
Total	99.04	99.09	100.12	98.88	98.95	99.9	99.77	99.21	97.73	99.21	99.98	99.83	99.55	99.47	99.89
Si	2.71	2.68	2.72	2.7	2.65	2.67	2.71	2.7	2.994	2.985	2.72	2.73	2.83	2.999	2.999
Al	1.28	1.31	1.27	1.28	1.32	1.31	1.28	1.28	0.994	1.005	1.26	1.26	1.16	0.99	0.99
Fe^{2+}	0.01	0.01	0.01	0.01	0.01	0.01	0	0.01	0.004	0.006	0.01	0.01	0.01	0.003	0.005
Ca	0.3	0.33	0.28	0.31	0.37	0.35	0.29	0.31	0.003	0	0.3	0.28	0.19	0.002	0
Na	0.69	0.67	0.7	0.68	0.66	0.66	0.69	0.69	0.159	0.139	0.7	0.71	0.82	0.15	0.12
K	0.02	0.02	0.02	0.02	0.02	0.02	0.01	0.02	0.865	0.886	0.03	0.03	0.02	0.88	0.9
Ab	68.4	65.8	69.8	66.8	63.2	64.2	69.5	67.5	15.5	13.6	68.5	70	79.8	14.3	11.9
An	29.9	32.7	27.9	30.9	35.3	34.4	29.3	30.6	0.3	0	29	27.1	18	0.2	0
Or	1.7	1.6	2.2	2.3	1.5	1.5	1.2	1.9	84.2	86.4	2.5	2.9	2.1	85.5	88.1

Two fractions of titanite with variable sizes yield two distinct data points. The oldest one has a $^{206}Pb/^{238}U$ age of 29.74 ± 0.39 Ma (Fig. 9b) overlapping within error the zircon age. The younger titanite has a $^{206}Pb/^{238}U$ age of 28.62 ± 0.39 Ma, which could reflect the thermal overprints during emplacement of the dykes (Fig. 9b).

5.4.3. Monzodiorite dyke sample K-7

This sample was collected from a ∼ 2 m thick monzodiorite dyke located inside the pluton. It mainly consists of brown hornblende and plagioclase with subordinate K-feldspar and accessory zircon and apatite. The sample yielded just few zircon grains, small, euhedral and translucent (Fig. 10a). Three fractions selected for U-Pb dating included two long clean zircon prisms, two semi clean zircons, and one tip. One analysis yields an age of 37.4 ± 0.43 Ma, distinctly older than two other fractions that have overlapping $^{206}Pb/^{238}U$ ages with a mean of 29.02 ± 0.10 Ma, interpreted to date the time of emplacement (Table 6; Fig. 10a).

5.4.4. Dacitic dyke sample Z-R-45

Sample Z-R-45 was collected from a 1.5 m thick dyke located in the country rocks to the east of the Lakhshak pluton. It is dacite with a porphyritic texture, comprising plagioclase, K-feldspar, quartz, biotite and green hornblende phenocrysts (<4%). The accessory minerals are titanite, zircon and apatite.

Only two grains of zircon were found in the sample. One was short prismatic with elongation ratios of 3.3; while the other was long and subhedral with an elongation ratio of 1.8 (Fig. 10b). They yield $^{206}Pb/^{238}U$ ages of 27.96 ± 0.34 Ma and 45.25 ± 0.15 Ma, respectively. Two fractions of titanites with different sizes yield identical data defining an average $^{206}Pb/^{238}U$ age of 29.39 ± 0.65 Ma (Table 6; Fig. 10b). This age is marginally older than that of the younger zircon. This may indicate that the zircon grain has been affected by some Pb loss. The alternative is that the titanite crystallized early in the magmatic history, before the magma could reach Zr saturation during final emplacement and precipitate some zircon.

6. Thermobarometry, oxygen fugacity and water content

6.1. Monzodiorite dykes: pyroxene thermometry and barometry

Magma P-T conditions can be estimated using clinopyroxene–whole-rock pairs (Putirka et al., 2003). $K_D(Fe\text{-}Mg)^{cpx\text{-}liq}$ was obtained using a Microsoft Excel spreadsheet program made by Putirka (2008) to tests the equilibrium between the analyzed diopside with the whole-rock composition, which is 0.27, representing the equilibrium condition ($K_D(Fe\text{-}Mg)^{cpx\text{-}liq}$ = 0.27 ± 0.03; Putirka, 2008). The barometric and thermometric calculations for clinopyroxene in sample K-47 reveal pressures ranging from 8.1 ± 0.92 to 6.0 ± 0.82 kbar and temperatures ranging from 1153 ± 11 to 1137 ± 21 °C (Table 2).

6.2. Monzodiorite dykes: amphibole thermometry and barometry

Several geobarometers have been proposed for the pressure estimation of amphibole crystallization in volcanic and sub-volcanic environments (e.g., Johnson and Rutherford, 1989). Ridolfi and Renzulli (2012) used the content of Al and other cations to obtain P, T, ΔNNO, and H_2O with low uncertainties (T ± 23.5 °C; P ± 11.5%; ΔNNO ±0.37 log units; H_2O_{melt} ± 0.78 wt%) in calc– alkaline and alkaline magmas. Calculation with Eq. 1a of Ridolfi and Renzulli (2012) for pargasite in the monzodiorite dyke (sample K-47) yields crystallization pressures of 5.89 ± 0.46 to 8.07 ± 0.38 kbar and temperatures of 965 to 993 °C (Table 4, Fig. 11). The calculated temperatures are between the solidus of basaltic magmas (950 °C) and the liquidus temperature (1100 °C) of sample K-47 (Table 1) obtained from KWare Magma software (Wohletz, 2008).

Table 4

Representative composition of amphiboles in the Lakhshak pluton and related dykes.

Sample No	K-47 (Monzodiorite dyke)					Z-R-27 (Dacite dyke)															Sample No	Z-R-13 (Lakhshak granodiorite)			K-13 (Lakhshak granodiorite)					
Location	C	R				C1 ore	C2 &R	C-R	R1	R2	C1	C2	C3 Core	C-R C&R	R1	R2	C1	C2	R	Location				Dark zone	Bright zone	Bright zone	Dark zone		
SiO_2	39.03	39.73	37.09	39.3	39.45	43.56	43.92	42.76	44.02	44.36	42.71	42.07	43.04	42.13	42.32	42.12	42.92	44.58	43.13	SiO_2	48.07	47.24	46.12	50.05	45.82	46.55	47.79	50.5	46.01
TiO_2	3.82	3.53	3.18	3.8	3.7	2.47	2.31	2.48	2.32	2.52	3.1	3.1	2.87	2.85	2.77	2.73	2.52	1.6	2.36	TiO_2	1.02	1.18	1.17	0.72	1.29	1.22	1.17	0.65	1.32
Al_2O_3	13.55	13.29	14.63	13.6	13.79	10.94	10.93	11.31	10.62	10.49	11.4	11.81	11.15	11.52	11.69	11.53	11.13	9.02	11.06	Al_2O_3	5.81	6.69	6.95	4.75	7.49	7.2	6.63	4.45	7.62
Cr_2O_3	0.03	0.02	0.03	0	0.01	0.1	0.04	0.03	0.09	0.06	0.02	0.02	0.03	0.02	0.05	0.06	0.08	0.02	0.04	Cr_2O_3	0.02	0.02	0.01	0.08	0.01	0.02	0.03	0.03	0.01
FeO_t	10.52	10.6	15.47	10.63	10.08	11.87	11.75	12.99	11.67	11.24	11.91	12.3	11.68	13.41	12.96	13.32	12.48	15.88	13.56	FeO_t	13.59	13.86	14.33	12.94	15.4	14.43	13.93	12.45	15.11
MnO	0.12	0.13	0.19	0.12	0.09	0.15	0.22	0.19	0.18	0.15	0.16	0.14	0.14	0.15	0.19	0.17	0.21	0.42	0.19	MnO	0.56	0.55	0.5	0.65	0.58	0.59	0.58	0.61	0.58
MgO	13.47	13.67	9.92	13.31	13.98	13.89	14.42	13.15	14.64	14.63	13.63	13.43	14.21	12.95	13.31	12.83	13.66	11.77	13.13	MgO	13.67	13.19	13.23	14.71	12.3	12.66	13.34	15.14	12.63
CaO	12.16	12.49	11.93	12.13	12.42	11.09	11.05	11.16	11.22	11.29	11.17	10.81	11.46	11	11.26	11.31	11.19	11.45	11.05	CaO	11.46	11.7	11.7	12.03	11.59	11.87	11.9	11.96	11.72
Na_2O	2.06	2.1	2.15	2.11	2.1	2.19	2.18	2.27	2.18	2.13	2.3	2.34	2.27	2.29	2.3	2.28	2.27	1.76	2.14	Na_2O	1.26	1.41	1.33	0.9	1.38	1.36	1.15	0.86	1.47
K_2O	1.65	1.57	1.5	1.58	1.6	0.63	0.62	0.66	0.66	0.63	0.89	0.87	0.78	0.79	0.77	0.75	0.69	0.85	0.68	K_2O	0.43	0.5	0.57	0.43	0.76	0.67	0.56	0.41	0.81
Total	96.62	97.22	96.31	96.74	97.44	96.95	97.57	97.17	97.78	97.56	97.38	97.01	97.65	97.18	97.73	97.15	97.27	97.57	97.51	Total	95.96	96.49	95.91	97.38	96.82	96.65	97.18	97.21	97.43
[Si	5.87	5.93	5.74	5.9	5.87	6.44	6.45	6.37	6.46	6.5	6.32	6.26	6.34	6.29	6.27	6.29	6.37	6.69	6.41	[Si	7.18	7.05	6.95	7.33	6.9	6.97	7.08	7.38	6.87
Ti	0.43	0.4	0.37	0.43	0.41	0.27	0.26	0.28	0.26	0.28	0.35	0.35	0.32	0.32	0.31	0.31	0.28	0.18	0.26	Ti	0.11	0.13	0.13	0.08	0.15	0.14	0.13	0.07	0.15
Al	2.4	2.34	2.67	2.41	2.42	1.91	1.89	1.98	1.84	1.81	1.99	2.07	1.94	2.03	2.04	2.03	1.95	1.6	1.94	Al	1.02	1.18	1.23	0.82	1.33	1.27	1.16	0.77	1.34
Cr	0	0	0	0	0	0.01	0.01	0	0.01	0.01	0	0	0	0	0.01	0.01	0.01	0	0	Cr	0	0	0	0.01	0	0	0	0	0
Fe^{3+}	0	0	0	0	0	0	0	0	0	0	0	0	0	0	0	0	0	0	0	Fe^{3+}	0	0	0	0	0	0	0	0	0
Fe^{2+}	1.32	1.32	2	1.33	1.25	1.47	1.45	1.62	1.43	1.38	1.48	1.54	1.44	1.68	1.61	1.67	1.55	2	1.69	Fe^{2+}	1.7	1.73	1.81	1.59	1.94	1.81	1.73	1.52	1.89
Mn	0.02	0.02	0.02	0.02	0.01	0.02	0.03	0.02	0.02	0.02	0.02	0.02	0.02	0.02	0.02	0.02	0.03	0.05	0.02	Mn	0.07	0.07	0.06	0.08	0.07	0.07	0.07	0.07	0.07
Mg	3.02	3.04	2.29	2.98	3.1	3.06	3.16	2.92	3.2	3.2	3.01	2.98	3.12	2.88	2.94	2.86	3.02	2.63	2.91	Mg	3.04	2.93	2.97	3.21	2.76	2.83	2.94	3.3	2.81
Ca	1.96	2	1.98	1.95	1.98	1.76	1.74	1.78	1.76	1.77	1.77	1.72	1.81	1.76	1.79	1.81	1.78	1.84	1.76	Ca	1.83	1.87	1.89	1.89	1.87	1.9	1.89	1.87	1.88
Na	0.6	0.61	0.65	0.61	0.61	0.63	0.62	0.65	0.62	0.61	0.66	0.68	0.65	0.66	0.66	0.66	0.65	0.51	0.62	Na	0.37	0.41	0.39	0.26	0.4	0.4	0.33	0.24	0.42
K	0.32	0.3	0.3	0.3	0.3	0.12	0.12	0.13	0.12	0.12	0.17	0.17	0.15	0.15	0.15	0.14	0.13	0.16	0.13	K	0.08	0.1	0.11	0.08	0.15	0.13	0.11	0.08	0.15
P R & R, 2012 (kbar)	6.7	5.9	8.1	6.5	6.5	3.9	4.2	4.1	3.9	3.2	4.5	5.4	3.9	4.4	4.8	4.3	4.5	2.1	3.7	P Mutch et al., 2016 (kbar)	1.9	2.3	2.4	1.4	2.7	2.5	2.2	1.3	2.7
T R &R, 2012 (°C)	993	973	965	986	986	932	940	930	937	917	952	970	942	943	955	938	950	833	916	T Putirka, 2016 (°C)	760	782	788	733	789	787	771	728	798
Ni-NiO (fO2) R& R, 2012	−8.1	−8.8	−8.1	−8.1	−8.1	−10.4	−10.3	−10.4	−10.4	−10.7	−10.0	−9.4	−10.2	−10.1	−9.7	−10.2	−10.1	−12.6	−10.7	Holland and Blundy, 1994 (°C)	700	707	747	685	671	642	685	682	725
H2Omelt R& R, 2012 (%)	6.30	6.63	8.92	6.36	6.58	5.93	6.02	6.35	5.89	5.56	5.59	5.77	5.68	6.03	6.17	6.25	6.10	6.58	6.31	Ni-NiO (fO2) R& R, 2012	−14.3	−13.8	−13.8	−15.0	−13.4	−13.7	−14.1	−15.4	−13.2
																				H2Omelt R& R, 2012 (%)	4.95	5.36	5.54	4.59	5.84	5.71	5.21	4.49	5.91

Abbreviations: C1, 2, 3 = sequence from centre to margin of core; C-R = boundary core to rim; R1, 2, 3 = sequence from inner to outer rim.

P R & R, 2012 (MPa) = Pressures calculated by Eq. 1a of Ridolfi and Renzulli (2012); T R &R, 2012 (°C) = calculated by Eq. 1a of Ridolfi and Renzulli (2012).

Ni-NiO (fO2) R& R, 2012 = Oygen fugacity NNO buffer (logfO2) from Ridolfi and Renzulli's (2012) P-T calibrations. Ni-NiO = Nickel-Nickel Oxide H2Omelt R& R, 2012 (%) = Amphibole-only H2Omelt (%) by Ridolfi and Renzulli (2012).

Table 5

Rb-Sr and Sm-Nd isotope analyses of the Lakhshak pluton and dykes.

Sample	Rb	Sr	$^{87}Rb/^{86}Sr$	$^{87}Sr/^{86}Sr$	$(^{87}Sr/^{86}Sr)_i$	Sm	Nd	$^{147}Sm/^{144}Nd$	$^{143}Nd/^{144}Nd$	$(^{143}Nd/^{144}Nd)_i$	εNd_i	$T_{DM.2stg}$
Z-R-1	64.9	335.1	0.56	0.705828	0.705591	2.97	16.87	0.107	0.512614	0.512593	−0.12	0.823
Z-R-2	59.2	428.7	0.399	0.705057	0.704889	3.34	19.18	0.105	0.512179	0.512159	−8.6	1.489
Z-R-22	70.1	321.6	0.631	0.706078	0.705811	2.95	17.32	0.103	0.512596	0.512576	−0.47	0.85
Z-R-9	61.2	357.6	0.495	0.70586	0.705657	2.99	17.25	0.105	0.512566	0.512546	−1.08	0.897
Z-R-16	15.2	908.2	0.048	0.705341	0.705322	5.15	24.66	0.126	0.512735	0.512711	2.16	0.643
Z-SH	50.4	159.7	0.914	0.708134	0.707748	4.37	20.66	0.128	0.512451	0.512426	−3.39	1.08

Samples Z-R-1, Z-R-2 and Z-R-22 represent the Lakhshak pluton; Z-R-9 is a dacite dyke; Z-R-16 is a monzodiorite dyke; Z-SH is a green schist representing the country rocks.

6.3. Dacite dykes: amphibole thermometry and barometry

Using the Eq. 1a of Ridolfi and Renzulli (2012) we obtain pressures of 3.19–5.39 ± 0.46 kbar (except one point with 2.12 kbar, a small amphibole rimmed by biotite) and temperatures of 833–970 °C (average = 933 °C) (Table 4, Fig. 11).

6.4. Lakhshak pluton: amphibole thermometry and barometry

Mutch et al. (2016) revised the Al-in-hornblende barometer of Holland and Blundy (1994), based on new experimental data on magmatic amphiboles from a variety of granite bulk compositions at near-solidus temperature and pressure (0.8–10 kbar) conditions. This barometer is applicable not only to granitic rocks consisting of magnesio-hornblende, plagioclase (An$_{15-80}$), biotite, quartz, alkali feldspar, ilmenite or titanite, magnetite, and apatite, similar to the mineral assemblage in Lakhshak granodiorite, but also the mineral assemblage that crystallizes at temperatures close to the haplogranite solidus (725 ± 75 °C).

The amphibole–plagioclase thermometer applied to the Lakhshak granodiorites yields T = 642–747 °C (Table 4). The Mutch et al. (2016) barometer yields P = 1.3–2.7 ± 0.5 kbar (Table 4). The crystallization temperature of magnesio-hornblende, calculated with the Al-in-amphibole thermometer of Putirka (2016; Eq. 5), ranges from 728 to 798 ± 40 °C. These results partly overlap those obtained with the amphibole–plagioclase thermometer of Holland and Blundy (1994; T= 642-747 ± 40 °C) (Table 4, Fig. 11).

6.5. Oxygen fugacity and water content

Important factors in crystallization processes in magmatic rocks are oxygen fugacity (fO_2) and H_2O_{melt} content. Oxygen fugacity controls the pressure-temperature correlations in melts and affects the stability intervals for rock-forming minerals. This value generally increases as a function of increasing temperature.

The oxygen fugacity for monzodiorite dykes, based on Ni-NiO buffer (ΔNNO) values according to Ridolfi and Renzulli (2012), is nearly constant (−8.1 to −8.8), while it varies from −9.40 to 12.61 and −13.44 to 15.91 for dacite dykes and the Lakhshak granodiorites, respectively.

The H_2O_{melt} content is also estimated from amphibole compositions based on Ridolfi and Renzulli (2012) equation. It varies from 6.30 to 8.92%, 5.56 to 6.58 and 4.49 to 5.91 in monzodiorite dykes, dacite dykes and Lakhshak granodiorites, respectively. The high water (H_2O) content estimated for monzodiorite dykes is also confirmed by their higher percentage of amphibole (Fig. 3).

7. Discussion

7.1. Genetic classification of the Lakhshak rocks

On Harker variation diagrams, data from the plutons are separated from those of the dykes, but mostly show common trends of decreasing MgO, Fe$_2$O$_3$, CaO, MnO, TiO$_2$, Ba, Zr, Sr, Y and Yb with increasing SiO$_2$ (Figs. 5 and 6). The decrease of MgO, Fe$_2$O$_3$, Al$_2$O$_3$, CaO, MnO and TiO$_2$ in the pluton samples is due to fractionation of ferromagnesian minerals (e.g., hornblende and titanite). The P$_2$O$_5$ decreases with increasing SiO$_2$, presumably due to apatite fractionation, and suggests an I-type affinity (Fig. 5; He et al., 2018). The I-type affinity is also consistent with the presence of allanite and titanite. The decrease of Sr with increasing silica demonstrates that plagioclase and apatite were important fractionating phases (Fig. 6). Plagioclase fractionation is also confirmed by decreasing CaO and Na$_2$O with increasing SiO$_2$ (Fig. 5). The positive correlation of Rb and K$_2$O with silica indicates that biotite and K-feldspar were not early fractionation phases during evolution of the magma (Figs. 5 and 6).

Similar trends followed by two elements with almost the same partition coefficient from different groups of rocks suggest a cogenetic origin (Rollinson, 2014). This is the case for Yb vs. Y in the binary diagrams of incompatible elements (Fig. 12a), implying that the pluton and dyke samples are cogenetic. This is also supported by the parallel REE patterns. The REE contents decrease with increasing SiO$_2$: sample K-47 with 49.1 wt% SiO$_2$ (a monzodiorite dyke) has higher REE than sample Z-R-2 with 69.1 wt% SiO$_2$ (a granodiorite from the pluton) (Fig. 7a). This behaviour reflects the fact that minerals with high partition coefficient for the REE (e.g., apatite and amphibole) are less abundant in the Lakhshak granodiorites. All samples are characterized by very small negative Eu anomalies (Eu/Eu* = 0.78–0.87) and there is a systematic relationship between SiO$_2$ content and Eu/Eu* in which the ratio decreases with increasing SiO$_2$, suggesting fractionation of plagioclase (Table 1).

In the primitive mantle-normalized trace element diagram, all rocks show enrichment in large ion lithophile elements (LILEs) relative to high field strength elements (HFSEs) with prominent positive Pb and negative Nb anomalies (Fig. 7b). In addition, the granodiorites of the Lakhshak pluton have negative P and Ti anomalies, which are consistent with their lower abundance of apatite and titanite than in the monzodiorite dykes, confirmed through the petrography observation (see Sections 3.2 and 3.3). The Ti anomaly (Fig. 7b) may reflect an increase of the compatibility of Ti in the residue left by partial melting of water-bearing source rocks (Gaetani, 2004). The strong negative Nb and positive Pb anomalies of the Lakhshak granodiorites and dykes support an arc affinity (Fig. 7b) with parental magmas generated by partial melting of subducted oceanic lithosphere or contaminated mantle in a continental arc environment (e.g., Parlak and Robertson, 2004).

7.2. Adakitic connection

The Lakhshak granodiorites and the dykes plot in the field of adakites in the (La/Yb)$_N$ vs. Yb$_N$ and (La/Yb) vs. Yb diagrams (Fig. 12b and c).

It has been proposed (e.g., Tang et al., 2017; Wang et al., 2005) that adakites derived by partial melting of thickened mafic lower crust (≥55 km) are rich in K with K$_2$O > Na$_2$O and with high Th/U (average = 7), Th/Ba (0.04–0.08, average = 0.06), and Rb/Ba (0.15–0.35, average = 0.23). By contrast, the Lakhshak adakites are enriched in Na (K$_2$O < Na$_2$O) and have relatively low Th/U (3.3–7.8, average = 5.6), Th/Ba (0.01–0.02, average = 0.02), and Th/Ba (0.05–0.19, average = 0.11). Although continent–continent collision increases the crustal thickness,

Table 6

Zircon and titanite U-Pb data for the Lakhshak pluton and related dykes.

| Properties	Weight	U	Th/U	Pbi	Pbc	206/204	207/235	2 sigma	206/238	2 sigma	rho	207/206	2 sigma	206/238	2 sigma	207/235	2 sigma
	[ug]	[ppm]		[ppm]	[pg]			[abs]		[abs]			[abs]	[Ma]	[abs]	[Ma]	[abs]
(a)	(b)	(b)	(c)	(d)	(d)	(e)	(f)	(f, g)	(f)	(f)	(f)	(f,g)	(f)	(f,g)	(f)	(f)	(f)
Z-R-60 Lakhshak granodiorite																	
Zrn long clean	50	460	0.52	0.03	3.7	2036	0.03488	0.00014	0.005175	0.000012	0.73	0.04889	0.00014	33.272	0.077	34.814	0.142
Zrn tips	53	316	0.74	0.02	2.8	1753	0.03016	0.00015	0.004648	0.00001	0.64	0.04706	0.00019	29.897	0.066	30.17	0.15
Zrn long milky	56	339	0.85	0.02	3.1	1819	0.02997	0.00014	0.004649	0.000011	0.7	0.04676	0.00016	29.899	0.072	29.99	0.14
Ttn large	667	126	3.41	2.18	1422	36	0.02935	0.00191	0.004649	0.000018	0.52	0.04579	0.00289	29.897	0.117	29.37	1.88
Ttn small	571	126	3.76	2.2	1228	35.7	0.02895	0.00174	0.004634	0.000021	0.37	0.04531	0.00267	29.804	0.133	28.98	1.72
K-50 Lakhshak granodiorite																	
Zrn short part. milky	60	353	0.7	0.05	5	1471	0.03646	0.00017	0.005528	0.000013	0.7	0.04783	0.00016	35.539	0.085	36.36	0.16
Zrn long part. milky	83	349	0.77	0.01	2.6	3488	0.03274	0.0001	0.004982	0.00001	0.76	0.04766	0.0001	32.037	0.067	32.71	0.1
Zrn long clean	27	209	0.73	0.09	4.4	390	0.0303	0.00036	0.004662	0.000012	0.46	0.04713	0.00051	29.984	0.076	30.3	0.35
Ttn (~0.065 mm in size)	200	73	5.72	2.03	399	29.4	0.03284	0.00701	0.004624	0.000061	0.99	0.0515	0.0103	29.739	0.393	32.81	6.87
Ttn (~0.018 mm in size)	1465	83	5.34	2.1	3004	30.1	0.02601	0.00258	0.004449	0.000061	0.28	0.04241	0.00409	28.618	0.389	26.08	2.55
K-7 Monzodiorite dyke																	
Zrn 2 grain	1	943	0.66	0	0.5	666	0.03753	0.00081	0.005815	0.000066	0.59	0.04681	0.00082	37.376	0.425	37.41	0.79
Zrn tip 1grain	1	861	1.27	0	0.4	587	0.0293	0.00051	0.004531	0.000039	0.56	0.0469	0.00068	29.141	0.248	29.32	0.5
Zrn long	1	929	1.54	0	0.8	348	0.02882	0.00125	0.004507	0.000017	0.21	0.04638	0.00198	28.991	0.112	28.85	1.23
Z-R-45 Dacite dyke																	
Zrn SP 1grain AA	1	508	0.46	0	1.2	205	0.04659	0.0019	0.007044	0.000023	0.63	0.04797	0.00187	45.25	0.15	46.24	1.85
Zrn LP 1grain AA	1	496	0.5	0.01	2	85	0.02899	0.00321	0.004346	0.000053	0.48	0.04838	0.00512	27.955	0.338	29.02	3.16
Ttn small	191	93	0.92	1.9	357	32.8	0.03458	0.01588	0.0046	0.000212	0.73	0.05452	0.02334	29.588	1.36	34.52	15.47
Ttn large	61	89	0.82	1.72	104	33.5	0.0298	0.00715	0.004561	0.000115	0.09	0.04739	0.01136	29.333	0.739	29.81	7.03

a) Zrn = zircon (all zircon grains treated with chemical abrasion except for those marked with AA and for titanite (=Ttn), which were air abraded: fr = fragment; SP = short-prismatic; LP = long-prismatic.

b) Weight and concentrations are known to better than 10%, except for those near the ca. 1 μg limit of resolution of the balance.

c) Th/U model ratio inferred from 208/206 ratio and age of sample.

d) Pbi = initial common Pb; Pbc = total common Pb in sample (initial + blank).

e) Raw data, corrected for fractionation and spike.

f) Corrected for fractionation, spike, blank (206/204 = 18.3; 207/204 = 15.555) and initial common Pb (based on Stacey and Kramers, 1975); error calculated by propagating the main sources of uncertainty.

g) Corrected for 230Th disequilibrium according to Schärer (1984) and using Th/U magma = 6.8 for Z-R-60,5.4 for K-50-7, 7.8 for Z-R-45 and 3.8 for K-7-Z.

Table 7
Lead isotope analyses of feldspar and hornblende from Lakhshak rocks.

Sample No	Mineral	Weight	Pbt	U	Pb	$(^{206}Pb/^{204}Pb)_i$	2σ	$(^{207}Pb/^{204}Pb)_i$	2σ	$^{208}Pb/^{204}Pb$
		μg	ppm	ppm	ppm		%		%	
Lakhshak granodiorite										
K-50	Feldspar	790	19	0.055	18.32	18.776	0.1	15.693	0.2	39.167
Monzodiorite dyke										
K-7	Hbl (small)	489	1.6	0.19	1.82	18.731	0.1	15.655	0.2	39.073
K-7	Hbl (large)	597	1.8	0.21	1.59	18.717	0.1	15.648	0.2	39.025

Notes Hbl = hornblende; $(^{206}Pb/^{204}Pb)_i$ and $(^{207}Pb/^{204}Pb)_i$ are initial isotopic ratios corrected for fractionation, blank, and radiogenic Pb additions since 30 Ma; $^{208}Pb/^{204}Pb$ is corrected for fractionation and blank.
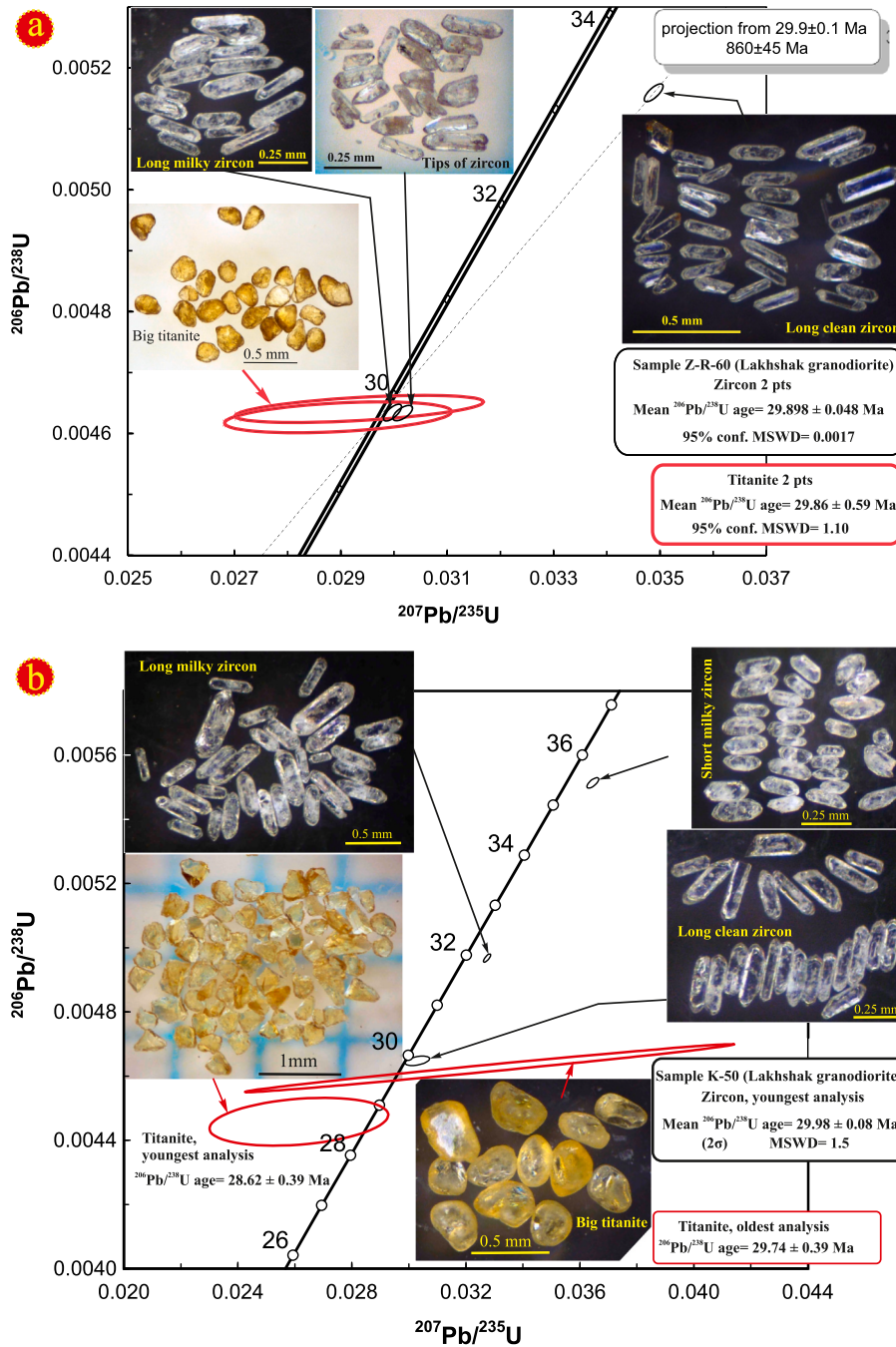
Fig. 9. (a) Concordia diagram showing the ID-TIMS U-Pb data and morphologies of zircon and titanite grains from Lakhshak granodiorite (sample Z-R-60). (b) Concordia diagram for Lakhshak granodiorite (sample K-50). Ellipses indicate the 2 sigma uncertainty.
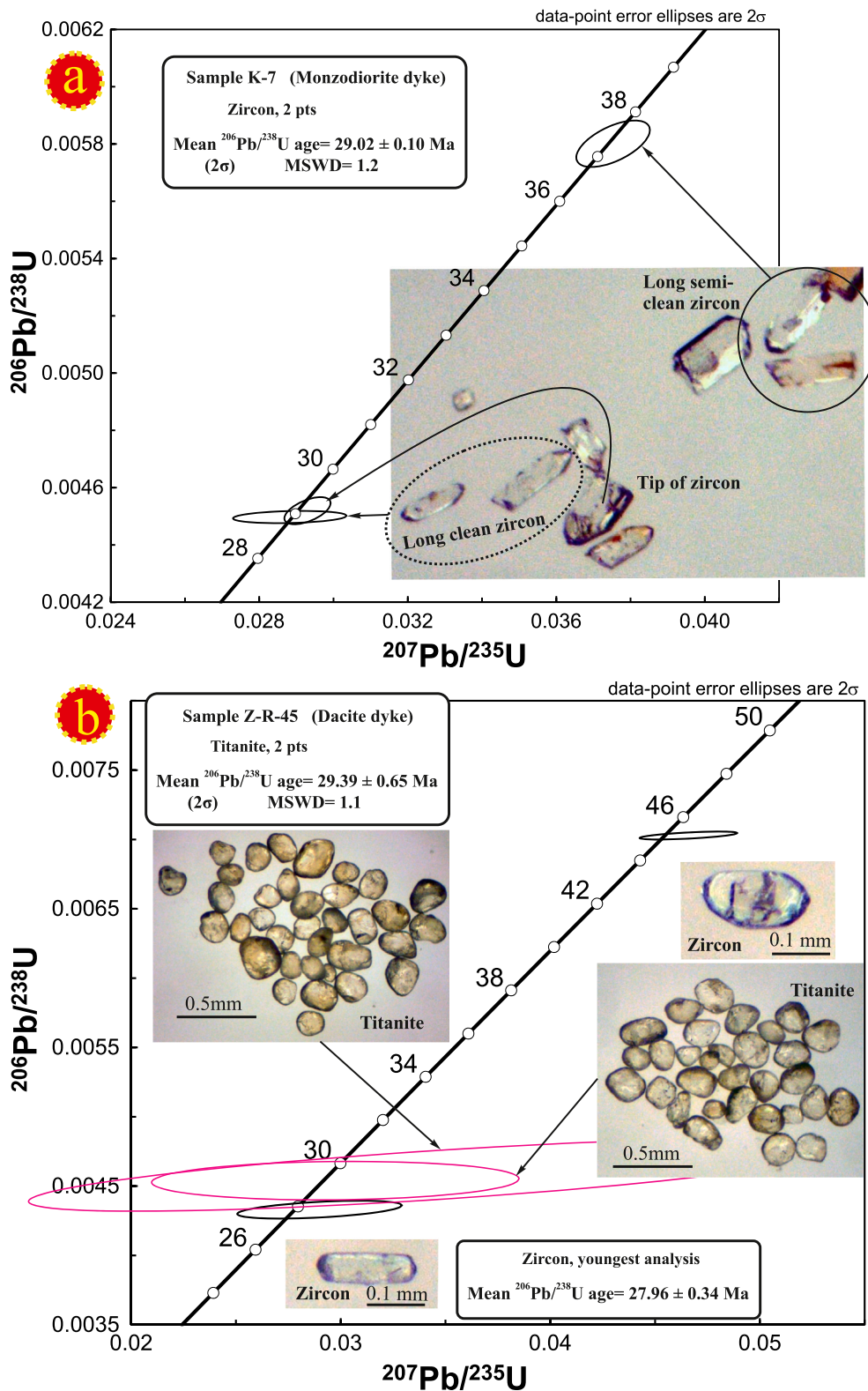
Fig. 10. (a) Concordia diagram showing the ID-TIMS U-Pb data and morphology of zircon from the monzodiorite dyke (sample K-7). (b) Concordia diagram with data and morphologies for zircon and titanite from the dacite dyke (sample Z-R-45).

the depth of the lower crust in the Zahedan region is estimate to be only ~38 km, based on geophysical data reported by Dehghani and Makris (1984). Considering that producing adakite rocks by melting of continental crust requires a thickness of >55 km (Wang et al., 2005), the adakite magmas of the Lakhshak pluton and the related dykes cannot

have originated by partial melting of amphibolitic lower crust.

Martin et al. (2005) pointed out that adakitic rocks formed by the fractionation of basaltic arc magma have lower SiO$_2$ concentrations (low-SiO$_2$ adakites) than those derived from melting of an oceanic slab (high-SiO$_2$ adakites). This also argues against crystallization of the
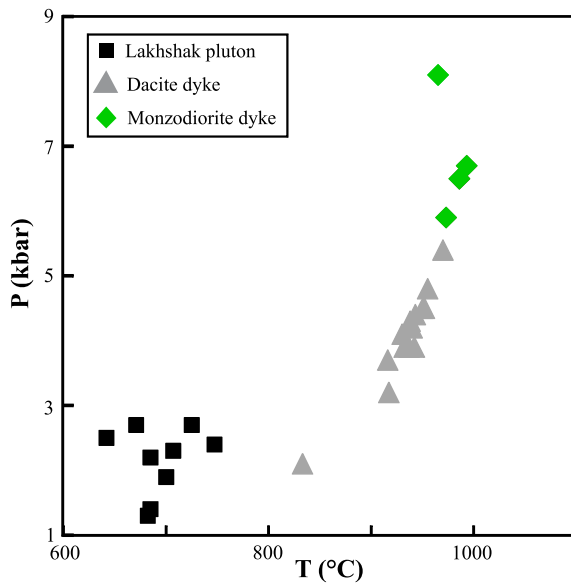
Fig. 11. Amphibole thermobarometry plot based on Ridolfi and Renzulli (2012), Mutch et al. (2016) and Putirka (2016). Data in Table 4.

adakite suite from basaltic arc magmas.

In the (La/Yb)$_N$ vs. Yb$_N$ diagram (after Drummond et al., 1996), the data fall in the field of adakites, between rocks originating from 10 to 25% melting of garnet amphibolite (Fig. 12b), indicating that garnet was left as residue in the source during the partial melting process. This is also confirmed by the low Yb contents (Table 1), since in andesite melts garnet and amphibole have high partition coefficients for Yb of 53 and 2, respectively (Rollinson, 2014).

Ribeiro et al. (2016) argue that slab melting is not necessarily required for producing high-SiO$_2$ adakites in hot subduction zones. They propose two possibilities. (1) Water-rich mantle melts stall and crystallize within lower and upper crustal magma storage regions to produce silica-rich melts with an adakitic signature- This is based on a case study in the Philippines. (2) Slab melts that percolate through the mantle wedge, mix or mingle with water-rich mantle melts within a lower crustal (~30 km depth) magma storage region, before their transfer to the upper arc crust (~7–15 km depth). This is based on a case study of Baja California. Based on the arguments mentioned above, the second process seems to be a better explanation for the origin of the Lakhshak adakites.

7.3. Isotopic constraints

In the (^{87}Sr/^{86}Sr)$_i$ vs. ε$_{Nd(t)}$ diagram (Fig. 13a), ε$_{Nd(t)}$ values for the dyke samples overlap those of the granodiorites of the Lakhshak pluton, but are distinctly different from their country rocks (sample Z-SH). This indicates that the dykes have a similar source to that of the granodiorites, as was inferred from the geochemical evidence discussed above (Figs. 7 and 12a). The Lakhshak adakite isotopic compositions are similar to those of the ophiolite and the basaltic rocks of the Ratuk Complex (the eastern part of Sistan Suture Zone), but distinct from those of normal lower continental crust (field is after Taylor and McLennan, 1985; Fig. 13a), thus more compatible with an origin by partial melting of Sistan oceanic lithosphere. As a comparison, the isotopic compositions of Aleutian adakites (Adak Island), which represent pure slab melts, overlaps in part with MORB. The Lakhshak compositions lie between those of MORB and that of the country rocks, indicating either mixing of these two end members, or derivation from a less juvenile mafic protolith. Mixing of mantle melts with assimilated turbidites has been suggested for the coeval Zahedan granites by Mohammadi et al. (2016b), based on variable zircon ε$_{Hf}$(T) values from +12 to −3. In the
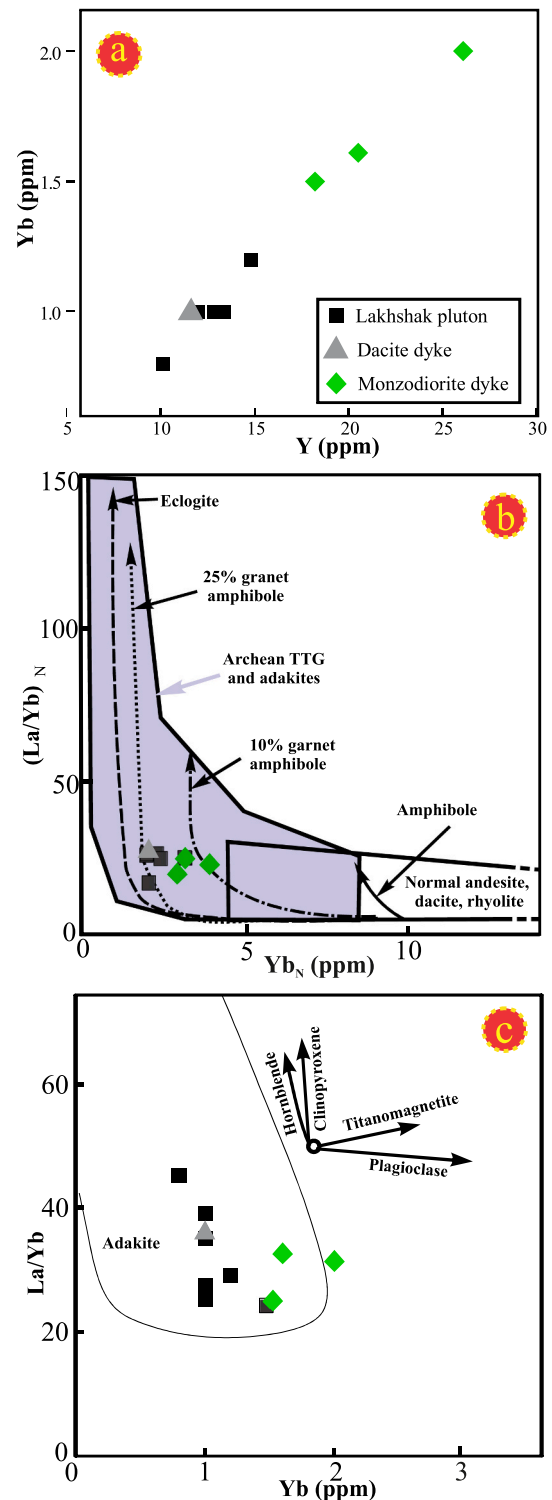

Fig. 12. (a) The common trend in the Yb vs. Y binary diagram suggests that the rocks are cogenetic. (b) (La/Yb)$_N$-Yb$_N$ diagram for the Lakhshak pluton and the related dykes. Fields of adakite and normal andesite, dacite and rhyolite (arc magmatic rocks) are from Drummond and Defant (1990). Four partial melting curves are displayed, two of which (amphibolite and 10% garnet amphibolite restite curves) assume a MORB source having Yb$_N$ = 10 and (La/Yb)$_N$ = 1 and the other two partial melting curves (eclogite and 20% hornblende eclogite curves) assume a MORB source with Yb$_N$ = 12 and (La/Yb)$_N$ = 1. (c) La/Yb-Yb diagram for the study samples. The arrays of mineral fractionations and adakite field are from Castillo et al. (1999).
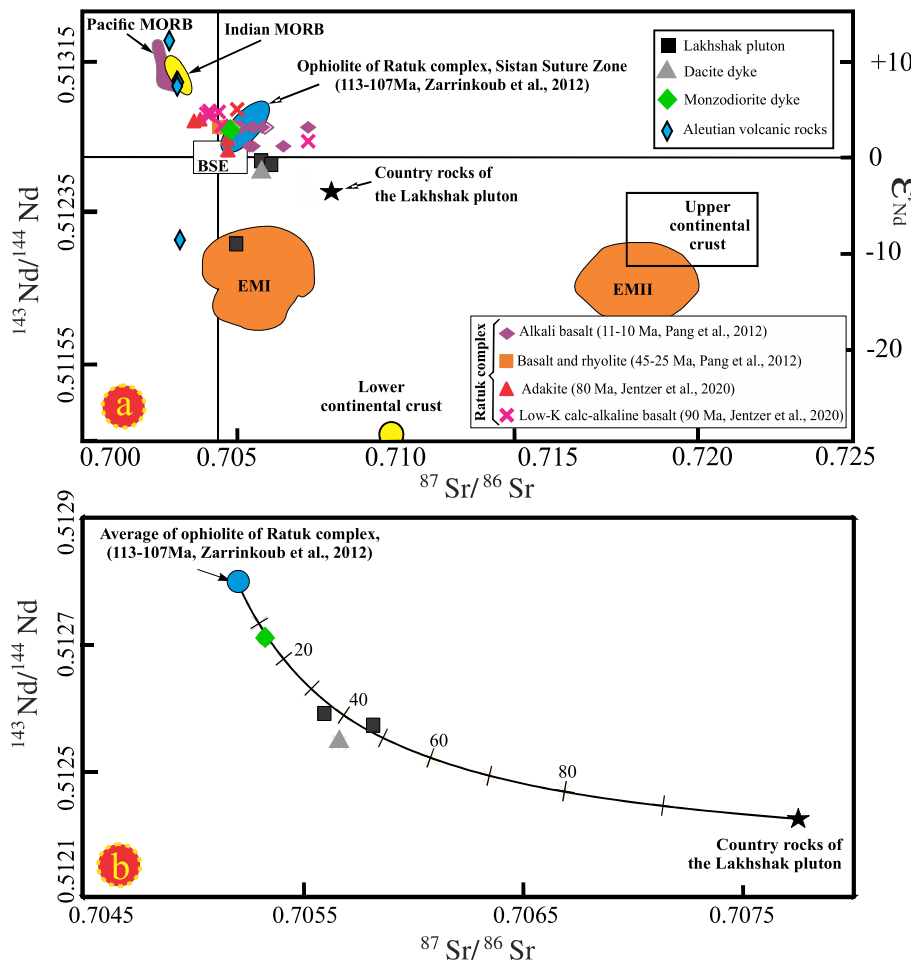
Fig. 13. (a) Sr-Nd isotope compositions. The Aleutian volcanic rocks were added to this binary diagram, since they are the classical example (data are from Jicha et al., 2004). EM-I (Enriched Mantle I; Lustrino and Dallai, 2003), EM-II (Enriched Mantle II; Workman et al., 2004), Bulk Silicate Earth (BSE; Rollinson, 2014), Indian MORB (Ito et al., 1987; Nauret et al., 2006), lower continental crust and upper continental crust (Taylor and McLennan, 1985), and Pacific MORB (Castillo, 2012). (b) The Lakhshak granodiorites and dykes plot on the mixing hyperbola. The mixing equations applied here are from Langmuir et al. (1978).
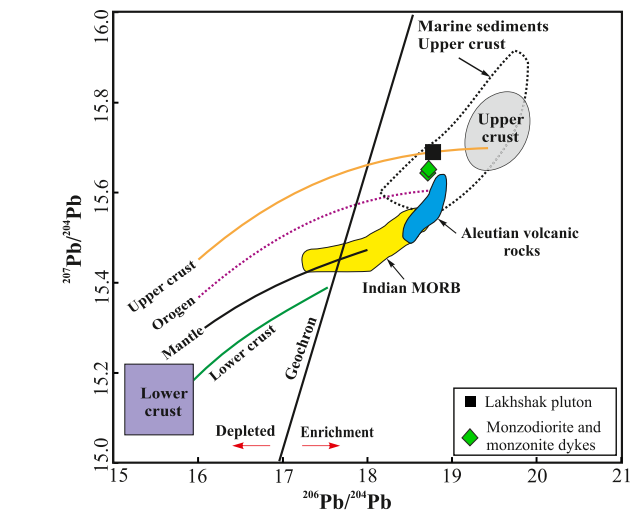
Fig. 14. Plumbotectonic model for Pb isotopic data. The Aleutian volcanic rocks (adakites) plot between Indian MORB and the Lakhshak adakites, suggesting a major role of recycled marine (pelagic) sediments or upper crustal materials in the genesis of the Lakhshak adakites. The Indian Ocean Ridge data are from Hamelin et al. (1986) and Aleutian lead isotopic data from Myers and Marsh (1987). The growth curves are from Zartman and Doe (1981).

$^{207}Pb/^{204}Pb$ vs. $^{206}Pb/^{204}Pb$ diagram the Aleutian volcanic rocks (adakites) plot between Indian MORB and the Lakhshak adakites (Fig. 14). Recycled marine (pelagic) sediments appear to have played a more

significant role in the genesis of the Lakhshak than the Aleutian adakites. This could have happened due to the slow subduction rate (2 cm/year), as for the Austral volcanic zone adakites from southern South America (Kay and Kay, 1993). This feature suggests that the combination of melting an oceanic slab and flysch sediments can account for the origins of the Lakhshak adakites. This is supported by the evidences for magma mixing and mingling textures such as quartz ocelli, acicular and mixed apatite morphologies in the Lakhshak pluton and dykes (Figs. 3c and e).

The mixing equation reported by Langmuir et al. (1978) are applied here to see how much each end-member had a role in the formation of the parent magmas of the Lakhshak site.

The mixing line suggests that the monzodiorite dyke can be produced through the combination of 86% magma from the oceanic slab with 14% from the country rocks, while the Lakhshak granodiorites and dacite dykes can be produce through mixing of 55–65% oceanic slab with 35–45% country rocks (Fig. 13b). This modeling shows that crustal contamination played a stronger role in the genesis of the Lakhshak granodiorites and dacite dykes than for the monzodiorite dykes.

7.4. Tectonic processes and the origin of adakites in the Neh Complex

Based on detrital zircon ages, Mohammadi et al. (2016a) suggested that collision between the Afghan plate and an intraoceanic island arc occurred at about 65 to 55 Ma, but the following evidence argues against this conception. (i) The presence of limestone containing microfossils of Early Eocene age in the Sefidabeh basin, 15 km away from the Lakhshak pluton, implies a closure of the Sistan Ocean after at most 56 Ma. (ii) The Sefidabeh basin has a marine sedimentary record with thousands of meters of turbidites of Middle-Late Eocene age (Tirrul et al., 1983; Burg,
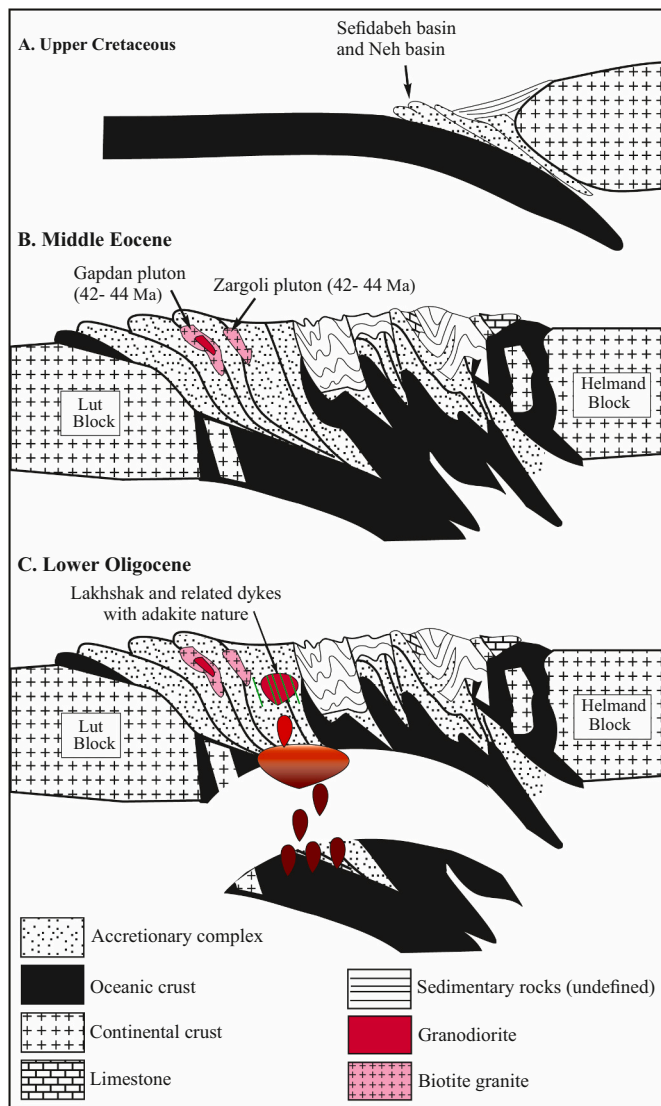
Fig. 15. Model for the tectonic evolution of the Sistan Suture Zone and generation of the Lakhshak pluton and dykes. The ages of Zargoli and Gapdan plutons are from Rezaei-Kahkhaei and Corfu (2013) and Rezaei-Kahkhaei et al. (2021), respectively.

2018; Fig. 15a). (iii) Molasse-type deposits formed during the Late Eocene–Early Oligocene thrusting and folding (Bagheri and Gol, 2020). The latter authors consider these sedimentary rocks to be late and/or post collisional, and conclude that the collision cannot have occurred before at most the beginning of the Late Eocene. They also point out that Early-Middle Eocene carbonate rocks in the Sistan Suture Zone were affected by the second phase of deformation (D₂; See Section 2.3 for more information about the deformation phases). Thus, the collision between the Lut and Helmand blocks, sandwiching the Neh Complex, probably occurred in the middle Eocene, at 44 to 42 Ma, when a number of biotite granitic plutons (Zargoli, Gapdan and Pircha) were emplaced in the Zahedan-Saravan magmatic belt (Fig. 15b). This event is registered by syntectonic emplacement fabrics formed in exhumed subduction-accretion prisms during the collision (Rezaei-Kahkhaei et al., 2010, 2021).

The zoned Gapdan pluton was emplaced in multiple stages at 44–42 and 30 Ma during progressive deformation and exhumation (Rezaei-Kahkhaei et al., 2021). At 44.31 ± 0.21 Ma the parent granitic magma crystallized at 4–5.4 ± 1 km depth; biotite and feldspar thermometers indicate crystallization temperatures of ~850 °C and ~730 °C,

respectively. This stage was tectonically controlled and the pluton was exhumed to shallower crustal levels of ~2.5 km, imparting a mylonitic fabric on the granite. At 42.15 ± 0.55 Ma granodiorite was emplaced in the center of the pluton at a depth of ~2.5 km. Crystallization depths are supported by the pressure estimates from Al-in-hornblende in rocks of the contact aureole.

The rapid uplift and voluminous magmatism between ~44 and ~30 Ma in the Sistan Suture Zone can have resulted from delamination (Fig. 15c). Zegers and van Keken (2001) suggest that delamination of a 10 km thick eclogitic layer would lead to 2 km of uplift and that the conducted and advected heat would cause magmatism within 10–20 m. y. after delamination. This is consistent with the geological evidence of the Neh Complex, where Sistan oceanic lithosphere was subcreted during the collision reaching a lithospheric thickness of 10 to 12 km. Delamination caused partial melting of the Sistan oceanic lithosphere producing the parent adakitic magmas of the Lakhshak pluton and related dykes.

The following model explains the tectonic evolution of the Neh Complex and generation of the Lakhshak adakites (Fig. 15). Around the middle Eocene the Sistan Ocean closed, and continental collision between the Lut and Helmand blocks along the Neh Complex caused the oceanic lithosphere to be subcreted at a low angle beneath the accretionary prims. Although delamination often produces C-type adakites (e. g., Li et al., 2013), in the Neh Complex this process produced adakites with characteristics similar to those formed by partial melting of subducted oceanic lithosphere. In fact, there is no evidence for the presence of continental crust beneath the Neh Complex. The delamination process caused partial melting of the young and warm Sistan oceanic lithosphere, resulting in voluminous basaltic magmas which might have settled at a pressure of ~8 kbar (based on pyroxene barometry; Table 2) at the Moho discontinuity depth (Figs. 14c). The underplated basaltic magmas started to differentiate via (1) the crystallization of pyroxene, amphibole, plagioclase, titanomagnetite, allanite and titanite and (2) mixing with melts from the accretionary prisms. This stage produced voluminous felsic magmas, which were then emplaced at 1.3–2.7 ± 0.5 kbar, and formed the granodioritic Lakhshak pluton (Fig. 15c; Table 4). Other magma batches formed the dykes, the dacite dykes corresponding to the granodiorites, and more primitive magma batches resulting in the monzodiorite dykes.

The compositions and thermometry results of clinopyroxene (diopside), amphibole (pargasite, magnesio-hastingsite and edenite; Fig. 8), and plagioclase demonstrate that the demise of the silicic magmatic system was characterized by sustained, high pre-injection magma temperatures in the magma chamber. Clinopyroxene compositions yield mean P and T values for the monzodiorite dykes of 6.8 ± 0.8 kbar and 1144 ± 21 °C (Table 2). These values are slightly higher than for the dacite/granodiorite dykes, thus denoting that diopside and pargasite in the monzodiorite dykes crystallized at higher pressures or crystallized prior to magnesio-hastingsite and edenite in the dacite dykes.

In the dacite dykes, some amphibole crystals display varying chemical composition across the zones. The P- T conditions, oscillatory zoning and repetitive resorptions are the result of new pulses of magma entering in the chamber. This is consistent with the observed resorption textures of plagioclase and quartz (Fig. 3c and e), as was observed in magma mixing models (Hiwatashi et al., 2021). The thermobarometry results also show that the amphiboles record a continuum of crystallization stages, starting early during magma ascent. Amphiboles crystallized as pargasite in the monzodiorite dykes followed by crystallization of magnesio-hastingsite in the dacite dykes, reflecting progressively decreasing P-T conditions from 1166 °C / 7.8 kbar to 933 °C / 4.0 kbar (Table 4; Fig. 11).

8. Conclusions

The Lakhshak suite consists of a granodioritic pluton with a medium granular texture, a set of rare intermediate to basic monzodiorite dykes,

and a set of more abundant dacitic dykes. The dykes are all porphyritic. The suite is calc-alkaline, metaluminous and I-type with elevated LILE and low HREE. The positive Pb anomaly and presence of older xenocrystic zircon reflect some involvement of crustal materials in the magma generation. Geochemical discrimination diagrams also reveal affinities with volcanic arc and post collisional granites.

Most dykes in the pluton lack chilled margins suggesting injection a short time after (or at a late stage in) the pluton emplacement. This is confirmed by U-Pb zircon and titanite geochronology that yields ages of 29.98 ± 0.1 and 29.80 ± 0.05 for the pluton, 28.95 ± 0.11 Ma for a monzodiorite dyke, and 29.4 to 27.96 Ma for a dacite dyke.

Integration of Sr, Nd, Pb and U-Pb ages with field studies, petrographic observations and geochemistry leads to the following conclusions for the genesis of the suite. In the middle Eocene the Sistan Ocean closed, and continental collision between the Lut and Helmand blocks led to underplating of the oceanic lithosphere underneath the accretionary prism. Delamination and heating caused partial melting of the warm Sistan oceanic crust producing adakitic magmas and also melting in the accretionary prism. Differentiation via the crystallization of clinopyroxene, amphibole, plagioclase ± magnetite formed voluminous intermediate to felsic magmas. The felsic magma of the accretionary prism mixed or mingled with these intermediate magmas, followed by emplacement in the upper crust at a depth of ∼7 km to form the Lakhshak pluton. Subsequent magma batches formed the monzodiorite and dacite dykes. The occurrence of disequilibrium textures, reaction rims and resorbed phenocrysts also supports the magma mixing hypothesis for genesis of the dykes.

Declaration of Competing Interest

The authors declare that they have no known competing financial interests or personal relationships that could have appeared to influence the work reported in this paper.

Acknowledgments

References

Aguillón-Robles, A., Calmus, T., Benoit, M., Bellon, H., Maury, R.C., Cotten, J., Bourgois, J., Michaud, F., 2001. Late Miocene adakites and Nb-enriched basalts from Vizcaino Peninsula, Mexico: indicators of East Pacific rise subduction below southern Baja California? Geology 29, 531–534.

Babazadeh, S.A., De Wever, P., 2004. Early Cretaceous radiolarian assemblages from radiolarites in the Sistan Suture (eastern Iran). Geodiversitas 26, 185–206.

Bagheri, S., Gol, S.D., 2020. The eastern Iranian orocline. Earth-Science Reviews 103322. https://doi.org/10.1016/j.earsc irev.2020.103322.

Bagheri, S., Stampfli, G.M., 2008. The Anarak, Jandaq and Posht-e-Badam metamorphic complexes in Central Iran: new geological data, relationships and tectonic implications. Tectonophysics 451, 123–155.

Berberian, M., 1983. The Southern Caspian: a compressional depression floored by a trapped, modified oceanic crust. Canadian Journal of Earth Sciences 20, 163–183.

Bonnet, G., Agard, P., Angiboust, S., Monie, P., Jentzer, M., Omrani, J., Whitechurch, H., Fournier, M., 2018. Tectonic slicing and mixing processes along the subduction interface: the Sistan example (Eastern Iran). Lithos 310, 269–287.

Bourdon, E., Eissen, J.P., Monzier, M., Robin, C., Martin, H., Cotten, J., Hall, M.L., 2002. Adakite-like lavas from Antisana Volcano (Ecuador): evidence for slab melt metasomatism beneath Andean Northern Volcanic Zone. Journal of Petrology 43, 199–217.

Boynton, W.V., 1984. Cosmochemistry of the rare earth elements: meteorite studies. In: Henderson, P. (Ed.), Rare Earth Element Geochemistry, pp. 63–114.

Bröcker, M., Rad, G.F., Burgess, R., Theunissen, S., Paderin, I., Rodionov, N., Salimi, Z., 2013. New age constraints for the geodynamic evolution of the Sistan Suture Zone, eastern Iran. Lithos 170, 17–34.

Burg, J.P., 2018. Geology of the onshore Makran accretionary wedge: Synthesis and tectonic interpretation. Earth-Science Reviews 185, 1210–1231.

Camp, V.E., Griffis, R.J., 1982. Character, genesis and tectonic setting of igneous rocks in the Sistan suture zone, eastern Iran. Lithos 3, 221–239.

Castillo, P.R., 2012. Adakite petrogenesis. Lithos 134, 304–316.

Castillo, P.R., Janney, P.E., Solidum, R., 1999. Petrology and geochemistry of Camiguin Island, southern Philippines: insights into the source of adakite and other lavas in a complex arc tectonic setting. Contributions to Mineralogy and Petrology 134, 33–51.

Corfu, F., 2004. U–Pb age, setting, and tectonic significance of the anorthosite–mangerite–charnockite–granite suite, Lofoten–Vesterålen, Norway. Journal of Petrology 45, 1799–1819. https://doi.org/10.1093/petrology/egh034.

Defant, M.J., Drummond, M.S., 1990. Derivation of some modern arc magmas by melting of young subducted lithosphere. Nature 347, 662–665.

Dehghani, G.A., Makris, J., 1984. The gravity field and crustal structure of Iran. Neues Jahrbuch für Geologie und Paläontologie (Abhandlungen) 168, 215–229.

Drummond, M.S., Defant, M.J., 1990. A model for trondhjemite-tonalite-dacite genesis and crustal growth via slab melting: Archean to modern comparisons. Journal of Geophysical Research - Solid Earth 95, 21503–21521.

Drummond, M.S., Defant, M.J., Kepezhinskas, P.K., 1996. Petrogenesis of slab-derived trondhjemite–tonalite–dacite/adakite magmas. Earth and Environmental Science Transactions of the Royal Society of Edinburgh 87, 205–215.

Fabries, J., Ferguson, A.K., Ginzburg, I.V., Ross, M., Seifert, F.A., Zussman, J., Aoki, K., Gottardi, G., 1988. Nomenclature of pyroxenes. Mineralogical Magazine 52, 535–550.

Gaetani, G.A., 2004. The influence of melt structure on trace element partitioning near the peridotite solidus. Contributions of Mineralogy and Petrology 147, 511–527.

Gao, S., Rudnick, R.L., Yuan, H.L., Liu, X.M., Liu, Y.S., Xu, W.L., Ling, W.L., Ayers, J., Wang, X.C., Wang, Q.H., 2004. Recycling lower continental crust in the North China craton. Nature 432, 892–897.

Hamelin, B., Dupré, B., Allègre, C.J., 1986. Pb-Sr-Nd isotopic data of Indian Ocean ridges: new evidence of large-scale mapping of mantle heterogeneities. Earth and Planetary Science Letters 76, 288–298.

He, Y., He, Z.H., Ge, W.C., Yang, H., Wang, Z.H., Dong, Y., Bi, J.H., Zhao, D., 2018. Petrogenesis and tectonic implications of Late Jurassic–Early Cretaceous granitic magmatism in the Xing'an Block, Northeast China: geochronological, geochemical, and Hf isotopic evidence. Canadian Journal of Earth Sciences 55, 571–588.

Hiwatashi, H., Ban, M., Álvarez-Valero, A.M., Kriegsman, L.M., Sato, M., 2021. Disequilibrium phenocrystic assemblage within dacites reveals magma mixing and stratified chamber after crustal assimilation at El Hoyazo volcano, SE Spain. Lithos 380, 105849.

Holland, T., Blundy, J., 1994. Non-ideal interactions in calcic amphiboles and their bearing on amphibole-plagioclase thermometry. Contributions to Mineralogy and Petrology 116, 433–447.

Ito, E., White, W.M., Göpel, C., 1987. The O, Sr, Nd and Pb isotope geochemistry of MORB. Chemical Geology 62, 157–176.

Jaffey, A.H., Flynn, K.F., Glendenin, L.E., Bentley, W.T., Essling, A.M., 1971. Precision measurement of half-lives and specific activities of ^{235}U and ^{238}U. Physical Review C 4, 1889–1906. https://doi.org/10.1103/PhysRevC.4.1889.

Jentzer, M., Whitechurch, H., Agard, P., Ulrich, M., Caron, B., Zarrinkoub, M.H., Kohansal, R., Miguet, L., Omrani, J., Fournier, M., 2020. Late cretaceous calc-alkaline and adakitic magmatism in the Sistan suture zone (Eastern Iran): Implications for subduction polarity and regional tectonics. Journal of Asian Earth Sciences 204, 104588.

Jicha, B.R., Singer, B.S., Brophy, J.G., Fournelle, J.H., Johnson, C.M., Beard, B.L., Lapen, T.J., Mahlen, N.J., 2004. Variable impact of the subducted slab on Aleutian island arc magma sources: evidence from Sr, Nd, Pb, and Hf isotopes and trace element abundances. Journal of Petrology 45, 1845–1875.

Johnson, M.C., Rutherford, M.J., 1989. Experimental calibration of the aluminum-in-hornblende geobarometer with application to Long Valley caldera (California) volcanic rocks. Geology 17, 837–841.

Jones, R.H., 1989. Ternary feldspars: Two-feldspar assemblages at P (H2O) = 5 kbar. Mineralogical Magazine 53, 347–355.

Kay, R.W., Kay, S.M., 1993. Delamination and delamination magmatism. Tectonophysics 219, 177–189.

Kolb, J., Thrane, K., Bagas, L., 2013. Field relationship of high-grade Neo-to Mesoarchaean rocks of South-East Greenland: Tectonometamorphic and magmatic evolution. Gondwana Research 23, 471–492.

Langmuir, C.H., Vocke Jr., R.D., Hanson, G.N., Hart, S.R., 1978. A general mixing equation with applications to Icelandic basalts. Earth and Planetary Science Letters 37, 380–392.

Li, X.H., Li, Z.X., Li, W.X., Wang, X.C., Gao, Y., 2013. Revisiting the "C-type adakites" of the Lower Yangtze River Belt, central eastern China: in-situ zircon Hf–O isotope and geochemical constraints. Chemical Geology 345, 1–15.

Ludwig, K.R., 2003. User's manual for Isoplot, v. 3.00, a geochronological toolkit for Microsoft Excel. In: Berkeley Geochronological Center Special Publication, 4, pp. 47–93.

Lustrino, M., Dallai, L., 2003. On the origin of EM–I end-member. Neues Jahrbuch für Mineralogie (Abhandlungen) 179, 85–100.

Martin, H., 1999. Adakitic magmas: modern analogues of Archaean granitoids. Lithos 46, 411–429.

Martin, H., Smithies, R.H., Rapp, R., Moyen, J.F., Champion, D., 2005. An overview of adakite, tonalite–trondhjemite–granodiorite (TTG), and sanukitoid: relationships and some implications for crustal evolution. Lithos 79, 1–24.

Mattinson, J.M., 2005. Zircon U–Pb chemical abrasion ("CA-TIMS") method: combined annealing and multi-step partial dissolution analysis for improved precision and accuracy of zircon ages. Chemical Geology 220, 47–66.

Middlemost, E.A., 1994. Naming materials in the magma/igneous rock system. Earth-Science Reviews 37, 215–224.

Mohammadi, A., Burg, J.P., Winkler, W., 2016a. Detrital zircon and provenance analysis of Eocene–Oligocene strata in the South Sistan suture zone, southeast Iran: implications for the tectonic setting. Lithosphere 8, 615–632.

Mohammadi, A., Burg, J.P., Bouilhol, P., Ruh, J., 2016b. U–Pb geochronology and geochemistry of Zahedan and Shah Kuh plutons, southeast Iran: Implication for closure of the South Sistan suture zone. Lithos 248, 293–308.

Molnar, P., England, P., 1990. Temperatures, heat flux, and frictional stress near major thrust faults. Journal of Geophysical Research - Solid Earth 95, 4833–4856.

Morimoto, N., 1988. Nomenclature of pyroxenes. Mineralogy and Petrology 39, 55–76.

Moyen, J.F., 2009. High Sr/Y and La/Yb ratios: the meaning of the "adakitic signature". Lithos 112, 556–574.

Mutch, E.J.F., Blundy, J.D., Tattitch, B.C., Cooper, F.J., Brooker, R.A., 2016. An experimental study of amphibole stability in low-pressure granitic magmas and a revised Al-in-hornblende geobarometer. Contributions to Mineralogy and Petrology 171, 1–27.

Myers, J.D., Marsh, B.D., 1987. Aleutian lead isotopic data: additional evidence for the evolution of lithospheric plumbing systems. Geochimica et Cosmochimica Acta 51, 1833–1842.

Nauret, F., Abouchami, W., Galer, S.J.G., Hofmann, A.W., Hémond, C., Chauvel, C., Dyment, J., 2006. Correlated trace element-Pb isotope enrichments in Indian MORB along 18–20 °S, Central Indian Ridge. Earth and Planetary Science Letters 245, 137–152.

Pang, K.N., Chung, S.L., Zarrinkoub, M.H., Mohammadi, S.S., Yang, H.M., Chu, C.H., Lee, H.Y., Lo, C.H., 2012. Age, geochemical characteristics and petrogenesis of Late Cenozoic intraplate alkali basalts in the Lut–Sistan region, eastern Iran. Chemical Geology 306, 40–53.

Pang, K.N., Chung, S.L., Zarrinkoub, M.H., Khatib, M.M., Mohammadi, S.S., Chiu, H.Y., Chu, C.H., Lee, H.Y., Lo, C.H., 2013. Eocene–Oligocene post-collisional magmatism in the Lut–Sistan region, eastern Iran: magma genesis and tectonic implications. Lithos 180, 234–251.

Parlak, O., Robertson, A.H.F., 2004. The ophiolite-related Mersin Mélange, southern Turkey; its role in the tectonic-sedimentary setting of Tethys in the Eastern Mediterranean region. Geological Magazine 141, 257–286.

Peccerillo, A., Taylor, S.R., 1976. Geochemistry of Eocene calc-alkaline volcanic rocks from the Kastamonu area, northern Turkey. Contributions to Mineralogy and Petrology 58, 63–81.

Putirka, K.D., 2008. Thermometers and barometers for volcanic systems. Reviews in Mineralogy and Geochemistry 69, 61–120.

Putirka, K., 2016. Amphibole thermometers and barometers for igneous systems and some implications for eruption mechanisms of felsic magmas at arc volcanoes. American Mineralogist 101, 841–858.

Putirka, K.D., Mikaelian, H., Ryerson, F., Shaw, H., 2003. New clinopyroxene-liquid thermobarometers for mafic, evolved, and volatile-bearing lava compositions, with applications to lavas from Tibet and the Snake River Plain, Idaho. American Mineralogist 88, 1542–1554.

Rezaei-Kahkhaei, M., Corfu, F., 2013. Igniting flare-up events in Sistan Suture Zone. Iran. Goldschmidt Conference abstract. Mineralogical Magazine 77, 2054.

Rezaei-Kahkhaei, M., Kananian, A., Esmaeily, D., Asiabanha, A., 2010. Geochemistry of the Zargoli Granite, Implications for development of the Sistan Suture Zone, southeastern Iran. Island Arc 19, 259–276.

Rezaei-Kahkhaei, M., Corfu, F., Sheykhi, M., Ghasemi, H., Shi, Y., 2021. Mineral chemistry and ages of the Eocene Gapdan granitoid pluton and related dykes (Sistan suture zone, eastern Iran): multi-stage emplacement of a zoned pluton during progressive deformation and exhumation. Journal of Asian Earth Sciences 216, 104813.

Ribeiro, J.M., Maury, R.C., Grégoire, M., 2016. Are adakites slab melts or high-pressure fractionated mantle melts? Journal of Petrology 57, 839–862.

Richards, J.P., Kerrich, R., 2007. Special paper: adakite-like rocks: their diverse origins and questionable role in metallogenesis. Economic Geology 102, 537–576.

Ridolfi, F., Renzulli, A., 2012. Calcic amphiboles in calc-alkaline and alkaline magmas: thermobarometric and chemometric empirical equations valid up to 1,130° C and 2.2 GPa. Contributions to Mineralogy and Petrology 163, 877–895.

Rollinson, H.R., 2014. Using Geochemical Data: Evaluation, Presentation, Interpretation. Routledge.

Sajona, F.G., Mauryr, Bellon, H., Cotten, J., Defant, M.J., 1996. High field strength element enrichment of Pliocene-Pleistocene island arc basalts, Zamboanga Peninsula, western Mindanao (Philippines). Journal of Petrology 37, 693–726.

Schärer, U., 1984. The effect of initial [230]Th disequilibrium on young U–Pb ages: the Makalu case, Himalaya. Earth and Planetary Science Letters 67, 191–204.

Stacey, J.S., Kramers, J.D., 1975. Approximation of terrestrial lead isotope evolution by a two-stage model. Earth and Planetary Science Letters 26, 207–221.

Sun, S.S., McDonough, W.F., 1989. Chemical and isotopic systematics of oceanic basalts: Implications for mantle composition and processes. In: Saunders, A.D., Norry, M.J. (Eds.), Magmatism in the Ocean Basins, 42. Geological Society, London, Special Publication, pp. 313–345.

Tang, G.J., Wang, Q., Wyman, D.A., Chung, S.L., Chen, H.Y., Zhao, Z.H., 2017. Genesis of pristine adakitic magmas by lower crustal melting: a perspective from amphibole composition. Journal of Geophysical Research - Solid Earth 122, 1934–1948.

Taylor, S.R., McLennan, S.M., 1985. The Continental Crust: Its Composition and Evolution. Blackwell Scientific Publications, Oxford (312 pp.).

Tirrul, R., Bell, I.R., Griffis, R.J., Camp, V.E., 1983. The Sistan Suture Zone of eastern Iran. Geological Society of America Bulletin 94, 134–150.

Vernon, R.H., 1984. Microgranitoid enclaves in granites — globules of hybrid magma quenched in a plutonic environment. Nature 309, 438–439.

Wang, Q., McDermott, F., Xu, J.F., Bellon, H., Zhu, Y.T., 2005. Cenozoic K-rich adakitic volcanic rocks in the Hohxil area, northern Tibet: lower-crustal melting in an intracontinental setting. Geology 33, 465–468.

Wang, S., Zhou, T., Yuan, F., Fan, Y., Cooke, D.R., Zhang, L., Fu, B., White, N.C., 2016. Geochemical characteristics of the Shujiadian Cu deposit related intrusion in Tongling: petrogenesis and implications for the formation of porphyry Cu systems in the Middle–Lower Yangtze River Valley metallogenic belt, eastern China. Lithos 252, 185–199.

Wang, X., Zhang, J., Rushmer, T., Adam, J., Turner, S., Xu, W., 2019. Adakite-like potassic magmatism and crust-mantle interaction in a postcollisional setting: an experimental study of melting beneath the Tibetan Plateau. Journal of Geophysical Research - Solid Earth 124, 12782–12798.

Wohletz, K., 2008. KWare Geological Software, 10th July 2008.

Workman, R.K., Hart, S.R., Jackson, M., Regelous, M., Farley, K.A., Blusztajn, J., Kurz, M., Staudigel, H., 2004. Recycled metasomatized lithosphere as the origin of the Enriched Mantle II (EM2) end-member: evidence from the Samoan Volcanic Chain. Geochemistry, Geophysics, Geosystems 5. https://doi.org/10.1029/2003GC000623ISSN: 1525-2027.

Yogodzinski, G.M., Kay, R.W., Volynets, O.N., Koloskov, A.V., Kay, S.M., 1995. Magnesian andesite in the western Aleutian Komandorsky region: implications for slab melting and processes in the mantle wedge. Geological Society of America Bulletin 107, 505–519.

Zarrinkoub, M.H., Pang, K.N., Chung, S.L., Khatib, M.M., Mohammadi, S.S., Chiu, H.Y., Lee, H.Y., 2012. Zircon U–Pb age and geochemical constraints on the origin of the Birjand ophiolite, Sistan suture zone, eastern Iran. Lithos 154, 392–405.

Zartman, R.E., Doe, B.R., 1981. Plumbotectonics - the model. Tectonophysics 75, 135–162.

Zegers, T.E., van Keken, P.E., 2001. Middle Archean continent formation by crustal delamination. Geology 29, 1083–1086.